PDF issue: 2024-06-13

Nonpolymer Organic Solar Cells: Microscopic Phonon Control to Suppress Nonradiative Voltage Loss via Charge-Separated State

Nagatomo, Takaaki ; Vats, Ajendra K. ; Matsuo, Kyohei ; Oyama, Shinya ; Okamoto, Naoya ; Suzuki, Mitsuharu ; Koganezawa, Tomoyuki ; Fuki,…

(URL)
https://hdl.handle.net/20.500.14094/0100483300

Nonpolymer Organic Solar Cells: Microscopic Phonon Control to Suppress Nonradiative Voltage Loss via Charge-Separated State

Takaaki Nagatomo, Ajendra K. Vats, Kyohei Matsuo, Shinya Oyama, Naoya Okamoto, Mitsuharu Suzuki, Tomoyuki Koganezawa, Masaaki Fuki, Sadahiro Masuo,* Kaoru Ohta,* Hiroko Yamada,* and Yasuhiro Kobori*

Read Online

ACCESS | Metrics & More | Article Recommendations | Supporting Information

ABSTRACT: Recent remarkable developments on nonfullerene solar cells have reached a photoelectric conversion efficiency (PCE) of 18% by tuning the band energy levels in small molecular acceptors. In this regard, understanding the impact of small donor molecules on nonpolymer solar cells is essential. Here, we systematically investigated mechanisms of solar cell performance using diketopyrrolopyrrole (DPP)−tetrabenzoporphyrin (BP) conjugates of C4-DPP−H_2BP and C4-DPP−ZnBP, where C4 represents the butyl group substituted at the DPP unit as small p-type molecules, while an acceptor of [6,6]-phenyl-C_{61}-buthylic acid methyl ester is employed. We clarified the microscopic origins of the photocarrier caused by phonon-assisted one-dimensional (1D) electron−hole dissociations at the donor−acceptor interface. Using a time-resolved electron paramagnetic resonance, we have characterized controlled charge-recombination by manipulating disorders in π−π donor stacking. This ensures carrier transport through stacking molecular conformations to suppress nonradiative voltage loss capturing specific interfacial radical pairs separated by 1.8 nm in bulk-heterojunction solar cells. We show that, while disordered lattice motions by the π−π stackings via zinc ligation are essential to enhance the entropy for charge dissociations at the interface, too much ordered crystallinity causes the backscattering phonon to reduce the open-circuit voltage by geminate charge-recombination.

KEYWORDS: organic solar cell, voltage loss, charge-separation, charge-recombination, phonon-assisted dissociation, time-resolved EPR
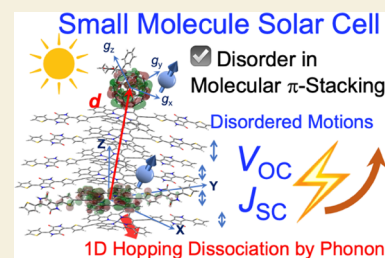
INTRODUCTION

Organic thin-film solar cells are expected to become the next generation of solar cells. Recently, their photoelectric conversion efficiency (PCE) has reached 18% by tuning the band energy levels in organic semiconductors.[1−6] Since small-molecule organic semiconductors can be purified, it is possible to control the crystalline packing structure with substituents to analyze the connection between thin-film structures and the photoelectric conversion mechanism. In this respect, further progress is expected in developments of small-molecule electron donors for high-performance nonpolymer solar cells because one can rationally manipulate the band energy level, vibration motion, and film morphology by a metal complexation or by introducing a substituent, as examples. The conversion of light energy to electrical energy proceeds through a five-step path.[3,7] Step 1: Absorption of light by donor and/or acceptor materials generates an exciton (a Coulombically bound electron−hole (e−h) pair). Step 2: The exciton diffuses into the interface of the donor and acceptor materials. Step 3: The charges are separated from the exciton. Step 4: The free charge carrier is transported toward the electrodes. Step 5: The charge carrier is injected into the electrodes. Optimization of each of the steps is important to improve the PCE values. After the charge-separation from the exciton to the hole−electron pair, the charge carriers should be transported to electrodes as free charges before geminate electron−hole recombination. An ideal active-layer compound for bulk-heterojunction (BHJ) organic photovoltaic devices (OPVs) forms the effective π−π stacking that facilitates exciton-diffusion[8,9] and charge-carrier transport.[10,11] It is also required to possess high-enough miscibility for forming sufficient heterojunctions to ensure efficient charge-separation.[12,13]
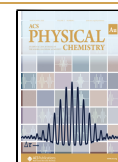
These characteristics are often not compatible in organic small-molecule semiconductors[14,15] and thus are challengeable in nonpolymer solar cells: compounds endowed with rich self-π−π interaction capacity tend to be poor in miscibility or maybe even insoluble in extreme cases. In particular, the lack of polymer chains will significantly restrict the carrier transport routes toward the electrodes, resulting in problematic recombination.[16] In 2017, Yamada et al. partially overcame this issue using a series of diketopyrrolopyrrole (DPP)−
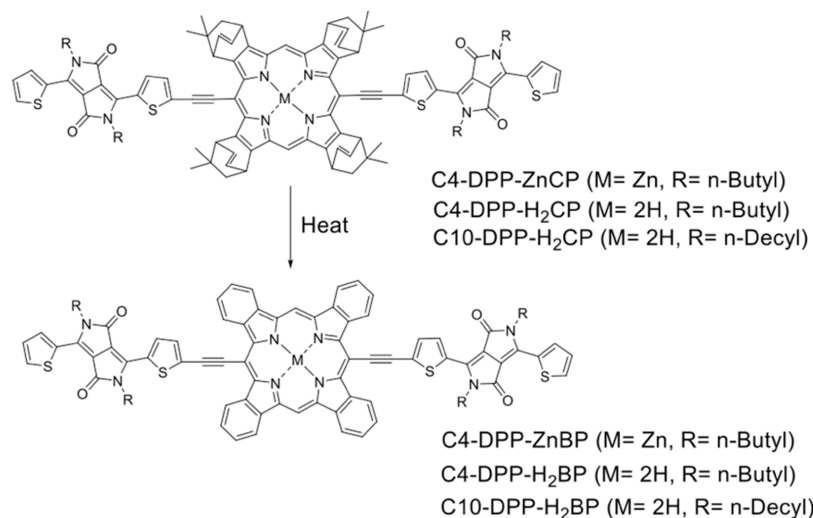
Scheme 1. P-type Semiconductors Prepared by the Thermal Precursor Approach

C4-DPP-ZnCP (M= Zn, R= n-Butyl)
C4-DPP-H₂CP (M= 2H, R= n-Butyl)
C10-DPP-H₂CP (M= 2H, R= n-Decyl)

Heat

C4-DPP-ZnBP (M= Zn, R= n-Butyl)
C4-DPP-H₂BP (M= 2H, R= n-Butyl)
C10-DPP-H₂BP (M= 2H, R= n-Decyl)

tetrabenzoporphyrin (BP) conjugates named Cn-DPP−H₂BP (n = 4, 6, 8, or 10 depending on the length of alkyl groups on the DPP unit) as a p-type material in BHJ OPVs in combination with [6,6]-phenyl-C$_{61}$-buthylic acid methyl ester (PC$_{61}$BM).[17] They used a precursor approach to prepare thin films of small-molecule organic semiconductors. For this, soluble precursor compounds are solution-processed into the thin-film form and then converted to target materials by quantitative in situ chemical reactions. The comparative study shows that the short-circuit current density (J_{SC}) largely depends on the length of alkyl substituents, ranging from 0.88 mA cm^{-2} (C10-DPP−H₂BP:PC$_{61}$BM) to 15.2 mA cm^{-2} (C4-DPP−H₂BP:PC$_{61}$BM) with PCE values of 0.19 and 5.2%, respectively. The introduction of shorter alkyl chains positively affected the miscibility and molecular orientation in terms of both the charge-carrier generation and transport efficiencies owing to the preferable morphology and π−π-stacking orientation in the BHJ layer. Ikoma et al.[18] clarified the electron−hole recombination and extraction for photocarriers in Cn-DPP−H₂BP:PC$_{61}$BM through transient photocurrent measurements. Cn-dependent J_{SC} was interpreted in terms of the orientation of Cn-DPP−H₂BP and the morphology of blend films.

Although several methods have been applied to elucidate the elementary processes of charge carriers in BHJ-OSCs, mechanistic details of nonradiative loss in the open-circuit voltage (V_{OC}) are poorly understood originating from interfacial heterogeneous electron−hole pairs.[19−24] A recent time-resolved electron paramagnetic resonance (TREPR) study suggested an impact of the recombination process generating the triplet excitons in nonfullerene acceptor solar cells,[25] while geometries and motions of charge-separated (CS) states were elucidated in details by electron spin polarization (ESP).[26−34] Furthermore, although effects of low-frequency nuclear motions (phonon) on photocarrier generations have been discussed in several studies,[28,34−39] the microscopic role of the phonon on OPV performance is unclear, including the impact of the phonon assist on primary recombination processes. Here, we combine microscopic and spectroscopic methods to elucidate the origins of charge-generation and recombination in BHJ-OSC with C4-DPP-benzoporphyrin conjugates as the small-molecule donors. We identify controlled lattice motion for improving the OPV performance.

For this, zinc porphyrin, C4-DPP−ZnBP, was newly synthesized (Scheme 1) and is applied for the BHJ-OSCs and for the spectroscopic measurements.

■ EXPERIMENTAL/METHODS

OPV Film and Device Fabrication

Thin films for the absorption and fluorescence measurements, the photoelectron spectrometry, and the TREPR were prepared by spin-coating of precursors on glass substrates, followed by heating at 200 °C for 10 min. Details are as follows (precursor: concentration of the solution, solvent, spin rate, heating temperature, and duration): C4-DPP−H₂CP (4.8 mg mL^{-1}, CHCl₃ (10% CS₂ v/v), 800 rpm for 40 s, 200 °C for 10 min) and C4-DPP−ZnCP (5.0 mg mL^{-1}, CHCl₃ (10% CS₂ v/v), 800 rpm for 40 s, 200 °C for 10 min). For the OPV devices C4-DPP−(M)CP:PC61BM (p-type material 3 mM and n-type material 4 mM (3.64 mg·mL^{-1}), 1:1.3 (w/w)), C4-DPP-H2-CP (4.8 mg·mL^{-1}), and C4-DPP−ZnCP (5.0 mg·mL^{-1}), 200 μL of the BHJ layer in the premix solution of CHCl₃, THF, and CS₂ was spin-coated at 800 rpm for 40 s, followed by thermal annealing at 200 °C for 10 min on a hot plate in a glovebox. Finally, Ca (10 nm, 1 Å s^{-1}) and Al (90 nm, 10 Å s^{-1}) were vapor-deposited at high vacuum (∼10^{-5} Pa) through a shadow mask that defined an active area of 4.0 mm². The typical OPV structure was [ITO/PEDOT: PSS (30 nm)/ C4-DPP−(M)BP: PC$_{61}$BM/Ca (10 nm)/Al (90 nm)]. J−V curves were measured using a Keithley 2400 source measurement unit under AM 1.5G illumination at an intensity of 100 mW cm^{-2} using a solar simulator (CEP-2000RP, Bunkoukeiki). The external quantum efficiency (EQE) spectra were obtained under the illumination of monochromatic light using the same system. The thickness of active layers was measured using a surface profiler (Kosaka Laboratory, ET200) after the OPV measurements. More details on the preparations and characterizations are described in the Supporting Information (SI).

Two-Dimensional Grazing-Incidence Wide-Angle X-ray Diffractometry (2D-GIWAXD)

The GIWAXD experiments were conducted at beamline BL19B2 in SPring-8 (Hyogo, Japan). The X-ray beam was monochromatized by a double-crystal Si(111) monochromator, and the X-ray energy was 12.398 keV (λ = 1 Å). The incident angle was set to 0.12° with a Huber diffractometer, and the sample-to-detector distance was about 174 mm. Diffracted X-ray from samples was recorded by an X-ray photon counting pixel detector (PILATUS 300 K, Dectris) for 30 s at room temperature.

Fluorescence Spectroscopy

The steady-state fluorescence spectra and the fluorescence decays were measured using a sample-scanning inverted confocal microscope (IX-71, Olympus) in combination with a ps-pulsed laser excitation at 470 nm (10.0 MHz, 90 ps FWHM, PicoQuant). The laser beam was introduced to the inverted microscope and focused on the sample by an objective lens (40×, NA 0.75, Olympus). The fluorescence from the sample was collected by the same objective lens and passed through a confocal pinhole (100 μm) and a long-pass filter (LP02-514RU, Semrock) to remove the excitation laser. Subsequently, half of the fluorescence was detected by a spectrometer (SpectraPro2358, Acton Research Corporation) equipped with a cooled CCD camera (PIXIS400B, Princeton Instruments) to measure the fluorescence spectra. The remaining half of the fluorescence was detected by an avalanche single-photon counting module (APD: SPCM-AQR-14, PerkinElmer). The signal from the APD was connected to a time-correlated single-photon counting (TCSPC) PC board (SPC630, Becker & Hickl) to measure the fluorescence decays.

Femtosecond Transient Absorption (TA) Spectroscopy

The excitation laser source was obtained from a Ti:sapphire regenerative amplifier, which generates a 100 fs pulse with a center wavelength of 800 nm. The output was split into two, which were used for optical excitation of the sample and white-light generation for the probe and reference pulses, respectively. A 400 nm pump pulse was generated in a 1 mm-thick BBO crystal. For probe pulses, we use a white-light continuum generated by focusing 800 nm pulse into a 4 mm-thick CaF_2 crystal. Time delays between pump and probe pulses were controlled by a motorized optical delay line. Spectra of both pump and reference pulses were measured by a prism-based polychromator and NMOS linear image sensors (S3901-256Q; Hamamatsu). More details are described in the Supporting Information.

TREPR Measurement

TREPR spectra were measured using a Bruker EMX X-band continuous-wave (CW) EPR spectrometer without magnetic field modulation at 80 K. The second harmonics of (532 nm) of a Nd:YAG laser (Continuum Minilite II, FWHM = 5 ns) were used for the light excitations. A laser depolarizer (SIGMA KOKI, DEQ. 1N) was placed between the laser exit and the microwave cavity. Temperature was controlled by a cryostat system (Oxford, ESR900) using liquid nitrogen as the cryogen. For the Q-band TREPR measurements, we employed a Q-band microwave bridge (Bruker ER051Q, 35 GHz) with a Q-band resonator (ER5106QT-W) equipped with the Bruker EMX system.

Computation of TREPR Data

Spin-polarized EPR spectra of the excited triplet states were numerically calculated based on the stochastic-Liouville equation (SLE) on the spin states of the CS states using MATLAB (The MathWorks) codes. Theoretical details are described in the Supporting Information.

■ RESULTS

Solar Cell Performance

C4-DPP−ZnCP and C4-DPP−H$_2$CP were prepared following the reported procedure via the thermal precursor approach (Scheme 1).[17] Thermogravimetric analysis showed that the thermally induced retro-Diels−Alder reactions from C4-DPP−ZnCP to C4-DPP−ZnBP would start around 120−170 °C (Figure S1). The highest occupied molecular orbital (HOMO) levels of C4-DPP−BPs were determined by photoelectron spectrometry as −5.0 eV (Figure S2). The optical absorption spectra of C4-DPP−ZnBP and C4-DPP−H$_2$BP thin films are shown in Figure S3. The optical band gaps ($E_{g,opt}$) are almost identical for these donors.

Solution-processed BHJ OPVs with a general device structure of [ITO/PEDOT:PSS/C4-DPP−ZnBP:PC$_{61}$BM/Ca/Al] were fabricated by the thermal precursor approach using C4-DPP−ZnCP as the precursor of C4-DPP−ZnBP, according to the procedure reported in the literature.[17] The detail of the procedure is shown in the SI. As a reference, [ITO/PEDOT:PSS/C4-DPP−H$_2$BP:PC$_{61}$BM/Ca/Al] was also prepared in the same way.

The current density−voltage (J−V) curves and external quantum efficiency (EQE) spectra of typical cells are shown in Figure 1, and averaged performance data are summarized in
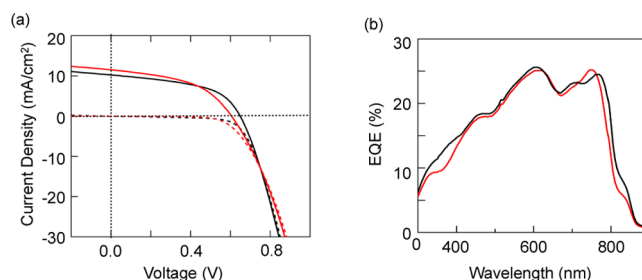
Figure 1. (a) Typical J−V curves of C4-DPP−H$_2$BP:PC$_{61}$BM (black lines) and C4-DPP−ZnBP:PC$_{61}$BM (red lines). Solid lines: in the light; dashed lines: in the dark. (b) EQE spectra of C4-DPP−H$_2$BP:PC$_{61}$BM (black lines) and C4-DPP−ZnBP:PC$_{61}$BM (red lines).

Table 1. Averaged Values of Photovoltaic Parameters of C4-DPP−H$_2$BP:PC$_{61}$BM and C4-DPP−ZnBP:PC$_{61}$BM OPVs[a]

| p-type materials	J_{SC} (mA cm^{-2})[c]	V_{OC} (V)[c]	fill factor[c]	PCE (%)[c]	ΔV_{OC} (V)[d]
C4-DPP−H$_2$BP[b]	10.8	0.62	0.41	2.7	1.03
C4-DPP−ZnBP[b]	11.0	0.60	0.43	2.8	0.86

[a]Obtained under AM 1.5G illumination at 100 mW cm^{-2}. [b]Active-layer thicknesses are 73 and 98 nm, respectively. [c]The respective standard deviations are as follows: δJ_{SC} = ±1.3 mA cm^{-2}, δV_{OC} = ±0.02 V, δFF = ±0.06, and δPCE = ±0.3% for C4-DPP−H2BP obtained by 26 cells. δJ_{SC} = ±0.7 mA cm^{-2}, δV_{OC} = ±0.01 V, δFF = ±0.03, and δPCE = ±0.3% by 23 cells. [d]Voltage loss estimated by $E_{CT}/q − V_{OC}$ in eq 3.

Table 1. Photovoltaic parameters of the best results are summarized in Figure S4, showing PCEs of 3.3% for C4-DPP−ZnBP:PC$_{61}$BM and C4-DPP−H$_2$BP:PC$_{61}$BM. The calculated J_{SC} from the EQE spectra in Figure 1b are 12.3 and 12.8 mA cm^{-2} for C4-DPP−ZnBP:PC$_{61}$BM and C4-DPP−H$_2$BP:PC$_{61}$BM, respectively. These roughly coincide with J_{SC}s in Figure 1.

Film Morphology, Crystallinity, and Disorder

Atomic force microscope (AFM) images of C4-DPP−ZnBP:PC$_{61}$BM and C4-DPP−H$_2$BP:PC$_{61}$BM films are shown in Figure S5, exhibiting restricted film roughness values of 1.79 and 2.05 nm, respectively.

The molecular arrangement in the C4-DPP−ZnBP neat film and the C4-DPP−ZnBP:PC$_{61}$BM blend film was analyzed by 2D-GIWAXD, in comparison with the corresponding C4-DPP−H$_2$BP neat film and the C4-DPP−H$_2$BP:PC$_{61}$BM blend film.[17] The 2D-GIWAXD images and their in-plane (a, c) and out-of-plane (b, d) profiles are shown in Figures 2 and 3, respectively. The neat film of C4-DPP−ZnBP shows
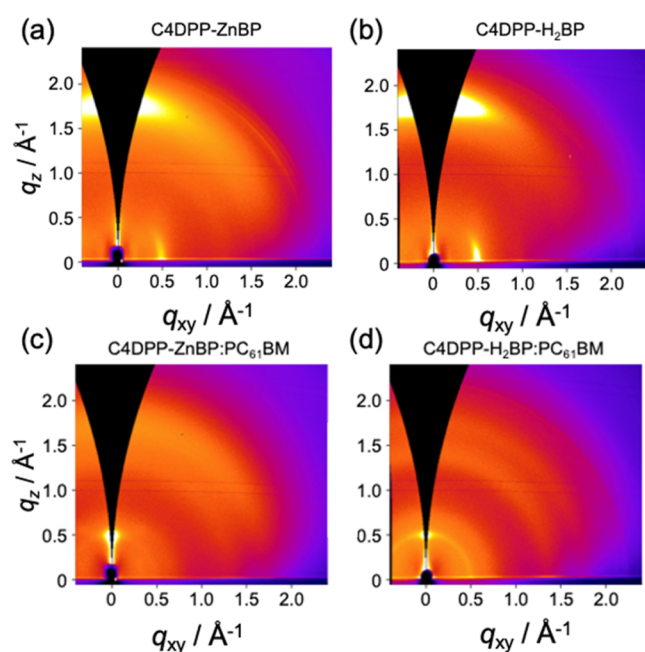
Figure 2. Two-dimensional GIWAXD images of (a) C4-DPP−ZnBP, (b) C4-DPP−H$_2$BP, (c) C4-DPP−ZnBP:PC$_{61}$BM, and (d) C4-DPP−H$_2$BP:PC$_{61}$BM.
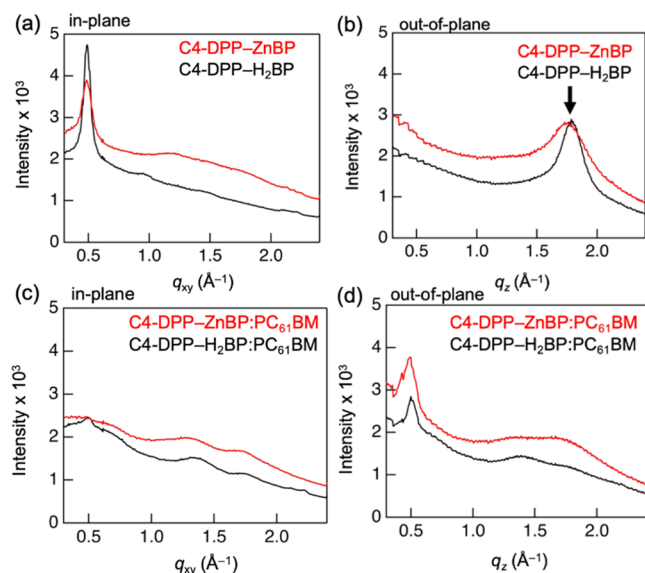
Figure 3. In-plane (a, c) and out-of-plane (b, d) profiles of 2D-GIWAXD images of (a, b) the C4-DPP−ZnBP (red) and C4-DPP−H$_2$BP (black) neat films and (c, d) the C4-DPP−ZnBP:PC$_{61}$BM and C4-DPP−H$_2$BP:PC$_{61}$BM (black) blend films.

combinations of a low-wavenumber diffraction in the in-plane direction (q_{xy} = 0.49 Å^{-1}, d = 13.0 Å) and a high-wavenumber diffraction in the out-of-plane direction (q_z = 1.76 Å^{-1}, d = 3.57 Å). The former diffraction corresponds to the edge-to-edge dimension of the BP framework and the latter to the $\pi-\pi$ stacking distance, similar to the C4-DPP−H$_2$BP neat film (Figure 2b).[17] The $\pi-\pi$ stacking distance (3.57 Å) of C4-DPP−ZnBP was longer than that of C4-DPP−H$_2$BP (3.51 Å). In addition, the broader peaks (see arrows in Figure 3b) of the C4-DPP−ZnBP film than those of C4-DPP−H$_2$BP suggest smaller crystallite sizes in C4-DPP−ZnBP than those in C4-DPP−H$_2$BP toward the out-of-plane directions.[40,41] Using the

Scherrer equation,[41] the mean crystallite sizes were estimated to be $r_{\pi\pi}$ = 1.4, 2.5 nm (Table 2), and 5.8 nm from the peak widths for the π-stacking directions in C4-DPP−ZnBP, C4-DPP−H$_2$BP, and C10-DPP−H$_2$BP,[17] respectively. The diffraction pattern of the C4-DPP−ZnBP:PC$_{61}$BM blend film is also similar to that of the C4-DPP−H$_2$BP:PC$_{61}$BM blend.

At around 1.35 Å^{-1}, a typical pattern of PC$_{61}$BM is observed (Figure 3c,d).[42] In the out-of-plane direction, edge-to-edge dimension of the BP framework (q_{xy} = 0.50 Å^{-1}, d = 12.6 Å) is observed. The in-plane profiles of the blend films also show a similar elongation of the $\pi-\pi$ stacking distance and shortening of the mean crystalline size by the zinc complexation (Figure 3c). The $\pi-\pi$ stacking distances were estimated to be 3.61 and 3.57 Å for C4-DPP−ZnBP and C4-DPP−H$_2$BP, respectively, from the peaks of the in-plane profiles (around 1.7 Å^{-1}) in their blend films (Figure 3c). The mean crystallite sizes were estimated to be $r_{\pi\pi}$ = 1.4 and 3.2 nm from the peak widths for the π-staking directions in the blend films of C4-DPP−ZnBP and C4-DPP−H$_2$BP, respectively. Thus, the broadened profiles in Figure 3d are not caused by disorders in the $\pi-\pi$ interactions by blending PC$_{61}$BM but by the additional diffractions from the PC$_{61}$BM clusters.
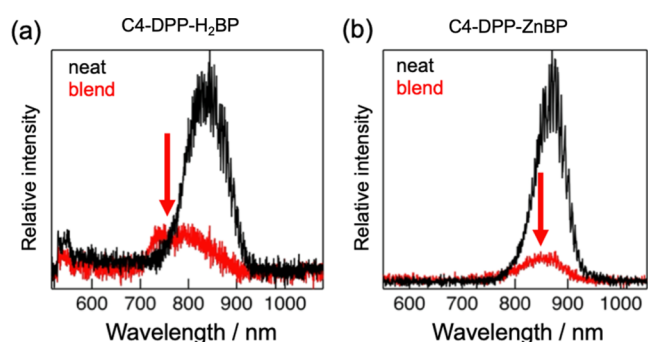
Fluorescence Spectroscopy

The fluorescence spectrum of the C4-DPP−H$_2$BP:PC$_{61}$BM blend film was measured (Figure 4a). Emission bands are observed around 750 nm in the blend films and at 830 nm in the neat film. In Figure 4a, the emission band is blue-shifted by blending PC$_{61}$BM. This would be caused by the hybridization between the charge-transfer exciton (^{1}CT*)[43] and the S$_1$ character before generating the trapped S$_1$ exciton in the donor domain by 470 nm excitations. The weak broad emission band at 850 nm of DPP−ZnBP:PC$_{61}$BM is also blue-shifted from the S$_1$ band of the neat film (Figure 4b). We performed theoretical calculations of the excited states of 1:1 molecular complexes of DPP−H$_2$BP:PC$_{61}$BM and DPP−ZnBP:PC$_{61}$BM using a time-dependent density functional theory (TDDFT) method (Figures S6 and S7). The ^{1}CT* state energies (E_{CT}) were estimated to be 1.65 and 1.46 eV for the DPP−H$_2$BP:PC$_{61}$BM and DPP−ZnBP:PC$_{61}$BM complexes, respectively. These are coincident with the CT emission positions (752 and 849 nm) in respective red spectra of Figure 4a,b in the blend materials. Time traces of the fluorescence intensity are observed as shown in Figure 5. The average fluorescence lifetime of the C10-DPP-H$_2$BP neat film is 0.34 ns, which is longer than the lifetimes of 0.30 ns of C4-DPP-H$_2$BP and C4-DPP-ZnBP. This is due to the larger crystalline size by the $\pi-\pi$ stacking of C10-DPP-H$_2$BP than that of C4-DPP-H$_2$BP, as reported previously.[17] From the neat film spectra in Figure 4, insertion of a low-pass (or short-pass) filter, which passes the fluorescence wavelength shorter than 760 nm, makes it possible to mainly obtain the ^{1}CT* emission decays (red traces in Figure 5).

The lifetime of ^{1}CT* emission of the C10-DPP−H$_2$BP:PC$_{61}$BM blend film is 0.38 ns, while those of C4-DPP−H$_2$BP:PC$_{61}$BM and C4-DPP−ZnBP:PC$_{61}$BM are 0.24 ns. As the 0.24 ns corresponds to the instrument response function, the ^{1}CT* generation and/or deactivation is faster than 0.24 ns, as identified by the transient absorption (TA) spectroscopy detailed below. The S$_1$ emission is significantly quenched in Figure 4 by blending PC$_{61}$BM, resulting in the predominant ^{1}CT* with a hybridized character (Figure S6). On the other hand, it is expected that these ^{1}CT* formations

Table 2. Parameters of the Geometries and Kinetics of the Photoinduced CS States to Account for the Delay Time-Dependences of the X-Band TREPR Spectra of the Triplet Excitons[a]

blend materials	D (mT)	J (mT)	Euler angles (α, β, γ) of $PC_{61}BM^{-\bullet}$ (degrees)[c]	dipolar angles (θ, ϕ) (degrees)	k_S (μs^{-1}) k_T (μs^{-1})[d]	T_{23} (μs)	(T_{1X}, T_{1Y}, T_{1Z}) (μs)[e]	$r_{\pi\pi}$ (nm)[f]
C4-DPP-H₂BP:PC₆₁BM[b]	−0.45 (±0.05)	0.30 (±0.02)	(20, 60, arbitrary)	(20 ± 10, 0)	1.0 / 4.0	0.7	(6.0, 0.5, 0.7)	2.5
C4-DPP-ZnBP:PC₆₁BM[b]	−0.47 (±0.05)	0.53 (±0.02)	(20, 20, arbitrary)	(20 ± 10, 0)	2.0 / 5.0	3.0	(10, 0.9, 0.5)	1.4

[a]The zero-field splitting (ZFS) parameters were employed as follows: $D_T = 0.0375$ cm^{-1} and $E_T = 0.0093$ cm^{-1} in C4-DPP-H₂BP and $D_T = 0.0380$ cm^{-1} and $E_T = 0.0098$ cm^{-1} in C4-DPP-ZnBP. See Figure S21 for possible errors. [b]In eq S26, anisotropic hyperfine couplings by four equivalent nitrogen atoms ($a_x = 0.01$ mT, $a_y = 0.01$ mT, $a_z = 0.12$ mT) were considered. Isotropic hyperfine couplings by six equivalent protons ($a_{iso} = 0.1$ mT) were considered for oxidized donors. $A_k = 0$ in $PC_{61}BM^{-\bullet}$. These EPR parameters were estimated by the density functional theory (DFT) calculations (see the Supporting Information in Figure S18). [c]X-convention with respect to the principal axis system (X, Y, Z) of the ZFS interaction. The listed angles are representative parameter sets relevant to the spin polarization obtained by summing the several anisotropic Δg contributions from the inhomogeneous conformation distributions. [d]T_+ populations were considered as quantum yields (Φ_+) of 0.10 and 0.02 via the $|S\rangle$-$|+\rangle$ mixings for C4-DPP-H₂BP:PC₆₁BM and C4-DPP-ZnBP:PC₆₁BM, respectively. [e]Anisotropy in the spin−lattice relaxation time of triplet exciton described in eq S24. [f]Mean crystallite size for the π-stacking direction obtained from the peak broadness in Figure 3b.

Figure 4. Steady-state fluorescence spectra of neat (black) and blend (red) films with PC₆₁BM of (a) C4-DPP-H₂BP and (b) C4-DPP-ZnBP. The red arrows show CT band positions, $E_{CT} = 1.65$ and 1.46 eV in (a) and (b), respectively, by the TDDFT methods (Figures S6 and S7).

take a few of 10 ps due to the exciton-diffusions in the crystalline regions. It is thus conceived that the picosecond decays do not reflect the $^1CT^*$ deactivation time but the waiting times for generating the $^1CT^*$ state. This is very consistent with the longer decay time constant (0.38 ns in Figure S8) in C10-DPP−H₂BP:PC₆₁BM than those (0.24 ns) in C4-DPP−H₂BP:PC₆₁BM and C4-DPP−ZnBP:PC₆₁BM; the grain size[17] of C10-DPP−H₂BP is larger than those in C4-DPP−H₂BP and C4-DPP−ZnBP. Thus, the $^1CT^*$ generation from S₁ is slower than those of C4-DPP−H₂BP:PC₆₁BM and C4-DPP−ZnBP:PC₆₁BM due to the exciton-diffusion time depending on the crystalline domain size. Overall, the intrinsic deactivation including the charge-separation process from the

$^1CT^*$ state would be quicker than the time constant of generating the $^1CT^*$ state, resulting in very weak emission bands.

To examine the $^1CT^*$ formation area in the blend films, fluorescence imaging maps were observed in Figure S9. Strong contrasts between the bright and dark spots of the micrometer domain sizes in C10-DPP-H₂BP:PC₆₁BM (Figure S9a) suggest existence of the large grains that inhibit the S₁ quenching processes. On the other hand, homogeneous distributions of the weak CT emission intensities indicate improved donor/acceptor (D/A) miscibility for the charge-separations in the blend films of C4-DPP-H₂BP:PC₆₁BM and C4-DPP-ZnBP:PC₆₁BM.

Femtosecond Transient Absorption Spectroscopy

To obtain detailed information on the early-time CT dynamics, we performed femtosecond TA measurements in the visible region. We also measured the TA spectra of the neat C4-DPP−H₂BP and C4-DPP−ZnBP films for comparison (Figure S10a,c). Figure 6a,b displays the temporal evolution of the absorbance changes (ΔA) in the C4-DPP−H₂BP:PC₆₁BM and C4-DPP−ZnBP:PC₆₁BM blend films with 400 nm excitation. In the neat films (Figure S10a,c), bleaching components were predominantly observed in the TA spectra, while strong positive absorption bands appeared only in the blend films around 500 nm (and 650 nm), as indicated by the solid arrows in Figure 6. Thanks to the intensity cancellation between the positive TA by the S₁ exciton and the negative ground-state bleaching (GSB) around the 500 nm region (Figure S10a,c), the signal intensities are very minor in the neat films, as shown at the bottom (blue traces) of Figure 6c,d.
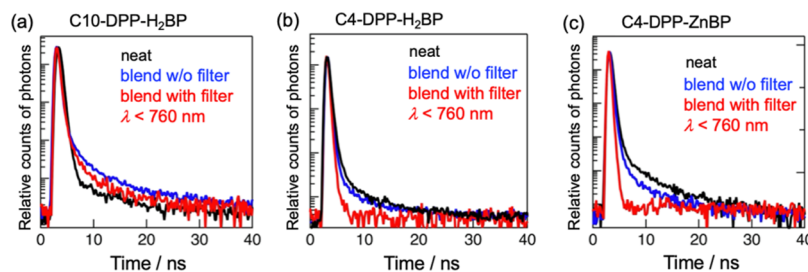
Figure 5. Fluorescence decay curves of neat films (black lines), blend films with PC₆₁BM (blue lines), and blend films with PC₆₁BM employing a low-pass filter (red lines) of (a) C10-DPP-H₂BP, (b) C4-DPP-H₂BP, and (c) C4-DPP-ZnBP. The bandpass filters cut the light over 760 nm to select the decays by the $^1CT^*$ emission.
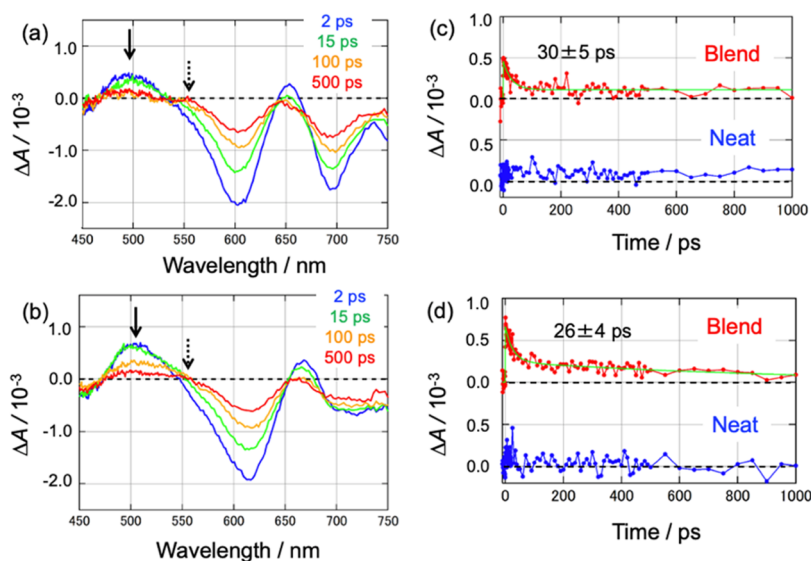
Figure 6. Temporal evolution of transient absorption spectra of the blend films of (a) C4-DPP−H$_2$BP:PC$_{61}$BM and (b) C4-DPP−ZnBP:PC$_{61}$BM. Time profiles of the absorbance changes in (c) C4-DPP−H$_2$BP:PC$_{61}$BM blend (red) and C$_4$-DPP−H$_2$BP neat (blue) films averaged at the 498−503 nm region and in (d) C4-DPP−ZnBP:PC$_{61}$BM blend and C$_4$-DPP−H$_2$BP neat films averaged at the 497−502 nm region. Excitation fluences were (a, c) 2.3 × 10^{15} photons/cm^2 and (b, d) 3.2 × 10^{15} photons/cm^2, respectively.
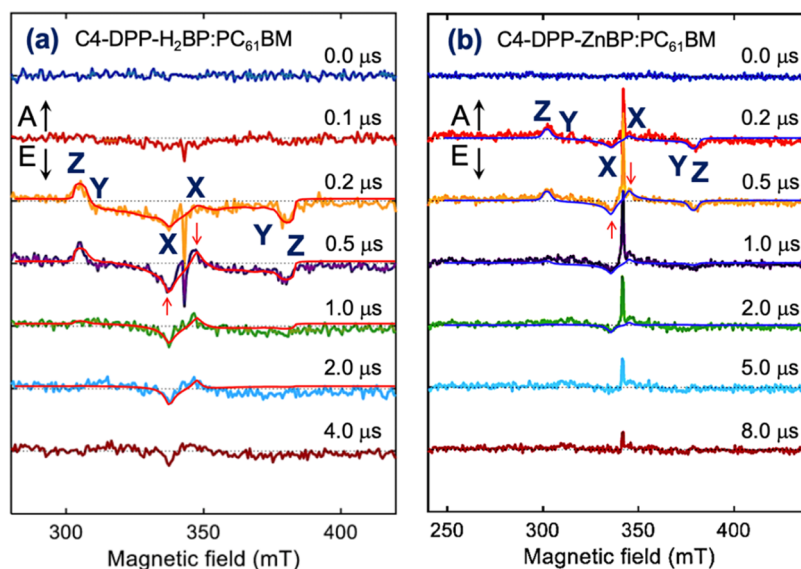

Figure 7. Delay time-dependences of the X-band TREPR spectra of (a) C4-DPP−H$_2$BP:PC$_{61}$BM and (b) C4-DPP−ZnBP:PC$_{61}$BM blend films observed by the 532 nm laser irradiations at 80 K. Simulated time-dependences of the triplet excitons are imposed by the red and blue lines, respectively. The decays in the Z and Y signal components were explained by the quick anisotropic spin−lattice relaxation times of T_{1Z} = 0.7 μs and T_{1Y} = 0.5 μs, respectively.

Thus, the positive signal components in Figure 6a,b can be assigned to the D/A interfacial excitons caused by blending PC$_{61}$BM, i.e., the fluorescent ^{1}CT* in Figure 4a,b.

From the red traces in Figure 6c,d, the decay time constants (ca. 30 ps) of the positive TAs are different from those observed in the initial decays of the GSB (Figures S11 and S12) in the neat films because of the intensity cancellation between the initial GSB and the S$_1$ exciton at 500 nm. In the blend films, we excite not only the donor molecules but also PC$_{61}$BM molecules using the 400 nm pulse. Therefore, this TA signal could have originated from PC$_{61}$BM. Keiderling and co-workers[44] found a strong TA at 550 nm in the neat PC$_{61}$BM films, which was assigned to the negative charge of PC$_{61}$BM but is different from the present TA bands (500 nm) in the

blend films. Moreover, the band peak position (solid arrow in Figure 6b) is red-shifted in the zinc porphyrin system with respect to the corresponding peak in the blend with the free-base porphyrin (Figure 6a). We thus conclude that these 500 nm bands originate from the interfacial ^{1}CT* states, while minor shoulder bands (dashed arrows in Figure 6) at 560 nm would be attributable to PC$_{61}$BM$^{-\bullet}$. It was difficult to identify the GSB component contributed by ^{1}CT* from the entire GSB dynamics of the blend materials (see Figures S10 and S11, and Tables S1 and S2.). This denotes that ^{1}CT* is a minor species with respect to the initial S$_1$ and to the CS products, indicating that the ^{1}CT* state in Figure 6 is immediately converted to the charge carriers, as discussed above. It is thus concluded that the S$_1$ exciton-diffusion corresponds to the 30 ps decays of the
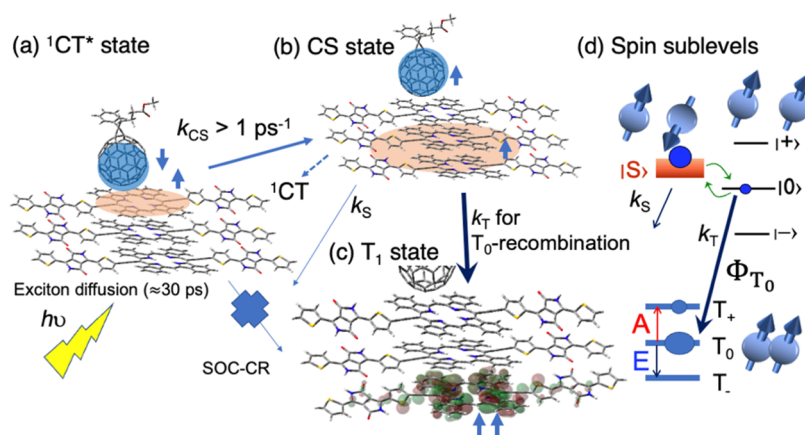
Figure 8. (a, b, c) Schematics of the photoinduced charge-separation and recombination causing losses in J_{SC} and V_{OC}. (d) Spin sublevel scheme from the interfacial CS state (upper) by the charge-recombination to the triplet exciton (bottom) in (c), resulting in the populations in the T_0 spins in the presence of the external magnetic field. A minor T_+ recombination loss is considered via the $|S>$-$|+>$ mixing.

^{1}CT* bands and that the charge-separation with $k_{CS} > 1$ ps^{-1} corresponds to the rise in the ^{1}CT* bands, as detailed in Figures S10−S13 with eq S1.[1] Therefore, ΔA at $t > 200$ ps in Figure 6c,d largely originates from the separated charge carriers, as shown in Figure S10. This charge-carrier density is proportional to the excitation fluence (Figure S14) and is not significantly altered by the zinc substitution.

Time-Resolved EPR Spectroscopy

To explore the origins of the voltages (V_{OC}) in Figure 1 in connection to microscopic geometries of the interfacial transient charge-separated (CS) states affecting the cell performances of (a) C4-DPP−H$_2$BP:PC$_{61}$BM and (b) C4-DPP−ZnBP:PC$_{61}$BM, we observed the TREPR spectra at 80 K of small cut films (Figure S15) in Figure 7. In Figure 7a,b, spin-polarized EPR signals by microwave absorption (A) and emission (E) are observed in the excited triplet states exhibiting zero-field splitting (ZFS), as indicated by X, Y, and Z. This splitting deviates from ZFS[44] of the triplet PC$_{61}$BM and thus is originating from the triplet exciton of the donors. The spin polarization exhibits $A/E/E/A/A/E$ patterns in the fine structures in (a) and (b) of Figure 7. This is not explained by the spin−orbit coupling-induced recombination[45] (SOC-CR in Figure 8) but by overpopulations of the T_0 sublevel (Figure 8d) in the triplet excitons via charge-recombination (CR)[26,33,46,47] of radical pairs (RPs) in the presence of the Zeeman interaction. The absence of SOC-CR strongly supports the quick dissociation kinetics ($k_{CS} > 1$ ps^{-1}) before the S-T spin-conversion in Figure 8a. Positive D values ($D_T = 0.0375$ cm^{-1} in C4-DPP−H$_2$BP and $D_T = 0.0380$ cm^{-1} in C4-DPP-ZnBP) in the ZFS parameters are conclusive from the polarization patterns and are consistent with the excitons localized in porphyrin monomers.[48] More details of the triplet characters are described in the Supporting Information with refs 47−49. Concerning the center field (340 mT) in Figure 7, sharp signal contributions are also observed and are from the charges by the interfacial charge-separations because g-value components ($g = 2.004$) from the radical cation of C4-DPP−H$_2$BP (C4-DPP−ZnBP) and $g = 2.000$ from the PCBM radical anion[50] appear using the X-band and Q-band TREPR methods (Figures S16−S18). In addition, the sharp contribution was not obtained at delay times larger than 0.5 μs in the neat C4-DPP−H$_2$BP film that exhibited a very weak emissive EPR signal only at 0.2 μs (Figure S19).

Notably, this sharp emissive spin polarization is minor in Figure 7a with respect to the contribution by the triplet exciton polarization at 0.5 μs. In contrast to this, a stronger sharp EPR signal around 340 mT is obtained in Figure 7b, while the triplet exciton signal is minor in the C4-DPP−ZnBP:PC$_{61}$BM blend film, suggesting that the charge-dissociation is more dominant in the Zn-substituted blend than in the free-base system at 80 K. This coincides with the lesser voltage loss (ΔV_{OC}) in Table 1 in the C4-DPP−ZnBP:PC$_{61}$BM device than in C4-DPP−H$_2$BP:PC$_{61}$BM, where ΔV_{OC} represents the potential difference between the ^{1}CT* state and V_{OC}, as detailed in the following section. This suggests that the triplet-recombination (k_T) in Figure 8 is a cause of the voltage loss.

In addition, emissive spin polarization was observed both in the triplet exciton and in the CS state in Figure 7a. These are explained by additional populations in the upper triplet sublevels ($|+>$ and T_+) in Figure 8d, suggesting that the mixing between the $|S>$ and $|+>$ states may also occur in the presence of a strong exchange coupling ($2J \approx g\beta B_0$) in Figure 8d.[51] Because J is required to be comparable to the hyperfine coupling to induce the populations in the $|0>$ and T_0 sublevels, heterogeneity in J-coupling is concluded to be higher for the interfacial CS states (Figure 8b) in the free-base donor systems than in the Zn-substituted blends. The involvement of the strong coupling of $2J = 340$ mT in C4-DPP−H$_2$BP:PC$_{61}$BM suggests that the averaged electronic coupling value by the CS and CT states is stronger to cause the preferential CR processes and thus is consistent with the stronger triplet exciton signals in Figure 7a. From the Q-band TREPR measurements at 80 K (Figure S20), the net emissive polarization was not obtained in the triplet exciton, denoting the absence of strong $2J$ exceeding 1.2 T in the CT state to resonate with the $|+>$ manifold at the high field. The inhomogeneous J-coupling also results in coexistence of the sharp CS-state signals and the broad T_0-populated triplets, particularly in Figure 7b, because the long-lived center signals persist longer than 8 μs, while the T_0-recombined triplet product appeared immediately at 0.2 μs. The origins of these inhomogeneities will be detailed in the Discussion section.

To determine geometries and J-couplings of the CS states possibly leading to losses in J_{SC} and V_{OC}, the density matrix formalism analysis[33] of the transient EPR spectra (red and blue fitting lines in Figure 7a,b) was performed, as shown in Figure 8d. We set tensor orientations of the principal axes of the g-
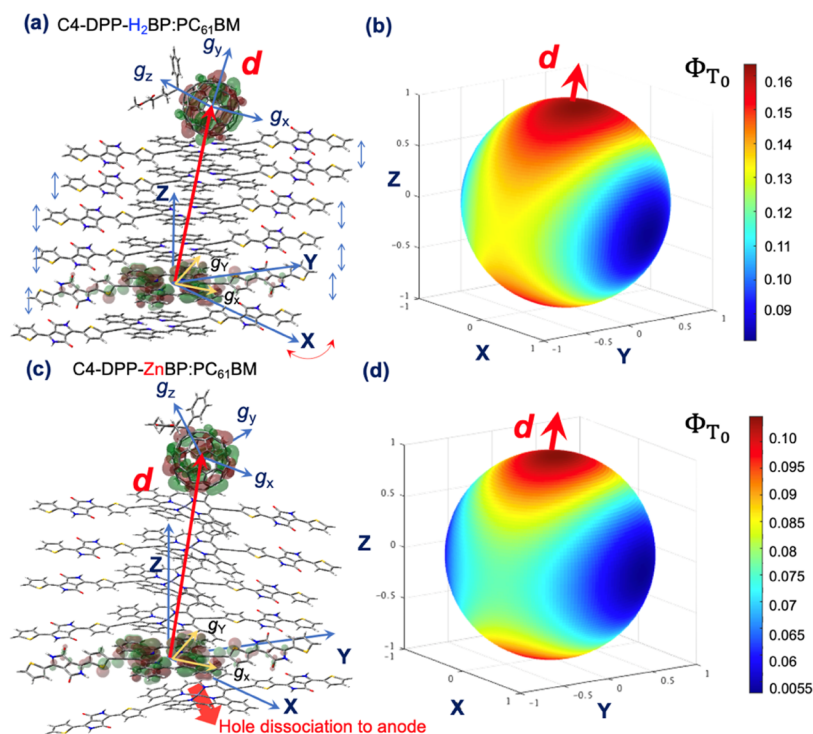
Figure 9. Geometries of the photoinduced CS states. (a, c): Settings of the g-tensor orientations of the principal axes in C4-DPP−H_2BP$^{+\bullet}$ (C4-DPP−ZnBP$^{+\bullet}$) and in PC$_{61}$BM$^{-\bullet}$. The axes of X, Y, and Z are the principal axes of the ZFS interactions of the triplet excitons. Vertical blue arrows in (a) represent collective intermolecular motions (phonon) by the ordered crystalline packing, causing $|S>$-$|0>$ dephasing during the charge-separations. Disorder of $\pi-\pi$ stacking in (c) results in charge dissociations. (b, d) Mapping of the T_0-sublevel yields (Φ_{T_0}) obtained by the density matrix formalism analysis at 0.2 μs, verifying the geometries of the distant CS state resulting in the T_0-recombination.

tensors ($g_X = 2.0036$, $g_Y = 2.0049$, and $g_Z = 2.0035$) in oxidized radical cations obtained by the density functional theory (DFT) calculation of B3LYP with 6-31G(d,p) basis sets (Figure S18) and in PC$_{61}$BM$^{-\bullet}$ ($g_X = 2.00085$, $g_Y = 2.00038$, and $g_Z = 1.99925$)[28] in the CS states with respect to the principal axes (X, Y, and Z) of the ZFS interactions in the triplet excitons (see Figure 9a and Table 2). In Figure 9a, the orientation of the principal axes of g_X and g_Y in the oxidized species is assumed to be rotated by 30 degrees from the orientation of the $X-Y$ planes of the triplet excitons. This is because the C=O bond direction in Figure S18 is anticipated to be close to the principal axis for $g_Y = 2.0049$ due to the spin−orbit coupling effect. The spin−spin dipolar couplings in the RP also possess anisotropy, causing the field direction (B_0) dependence of the $|S>$-$|0>$ conversion in Figure 8 because of the $|S>$-$|0>$ energy gap represented by $\Delta E_{ST} = 2d + 2J$,[52] where d $[=D(\cos^2 \theta_D -1/3)/2]$ is the spin−spin dipolar coupling with $D < 0$ as the dipolar coupling constant. θ_D is the angle between B_0 and the principal axis of the dipolar interaction, i.e., the interspin vector (d) in Figure 9a. From this, it is anticipated that the T_0 excitons are efficiently populated when $\theta_D = 0$ with $J > 0$ because the coherent $|S>$-$|0>$ conversions can occur due to the small ΔE_{ST}. This situation is fulfilled when the B_0 direction is parallel to the interspin vector. Therefore, the strong outer A/E spin polarization in the Z-transitions at 0.2 μs in Figure 7a denotes that the Z principal axis of the ZFS directs to the interspin vector between C4-DPP-H_2BP$^{+\bullet}$ and PC$_{61}$BM$^{-\bullet}$. The very weak E/A polarization for the X-transition indicates that θ_D is close to $\pi/2$, when B_0 is parallel to the short axis of X.

Based on the donor crystalline structures, the ^{1}CT* formations, and the quick charge-dissociation kinetics together with the above anisotropic $|S>$-$|0>$ conversions, we can assume the geometry model of the interfacial CS states, as shown in Figure 9a,c on the analysis of Table 2 by fitting the time-dependent EPR spectra.

Figure 9b shows the mapping of the T_0-yields for all possible directions obtained from the red line at 0.2 μs in Figure 7a, in which the Euler angles of the g_{PCBM} principal axis system are set to be $(\alpha, \beta, \gamma) = (20, 60°, \text{arbitrary})$ together with $(\theta, \phi) = (20, 0°)$ for the dipolar orientation in the $X-Y-Z$ system. Because the quantum yield (Φ_{T_0}) of the T_0 sublevel population in Figure 8d is determined by the anisotropic $|S>$-$|0>$ conversion and the singlet and triplet-recombination rate constants in the CS state,[52] it is anticipated that Φ_{T_0} is anisotropic, representing the anisotropic $|S>$-$|0>$ conversion efficiencies determined by the direction dependence of ΔE_{ST} and of the $|S>$-$|0>$ interaction to induce the spin-coherence by the Larmor frequency difference ($2Q_-$) between the radicals. More details on the principle are described in the SI with eq S26.[33] This triplet yield map is very consistent with the molecular conformation in Figure 9a, as detailed in the Supporting Information. The CS conformations (Figure 9a,c) are drawn based on the donor crystalline features with the $\pi-\pi$ stacking distances (0.35−0.36 nm from Figure 3b,d) and with the 1:1 donor:PC$_{61}$BM complex model (Figures S7 and S8). The interspin center-to-center separations of $r_{CC} = 1.8$ nm are obtained from $D = -0.45$ and -0.47 mT in the RPs in Table 2 using the point dipole approximation. $r_{CC} < r_{\pi\pi}$ (=2.5 nm in Table 2) in the C4-DPP−H_2BP:PC$_{61}$BM blend indicates that the hole is located in the crystalline environment as shown in
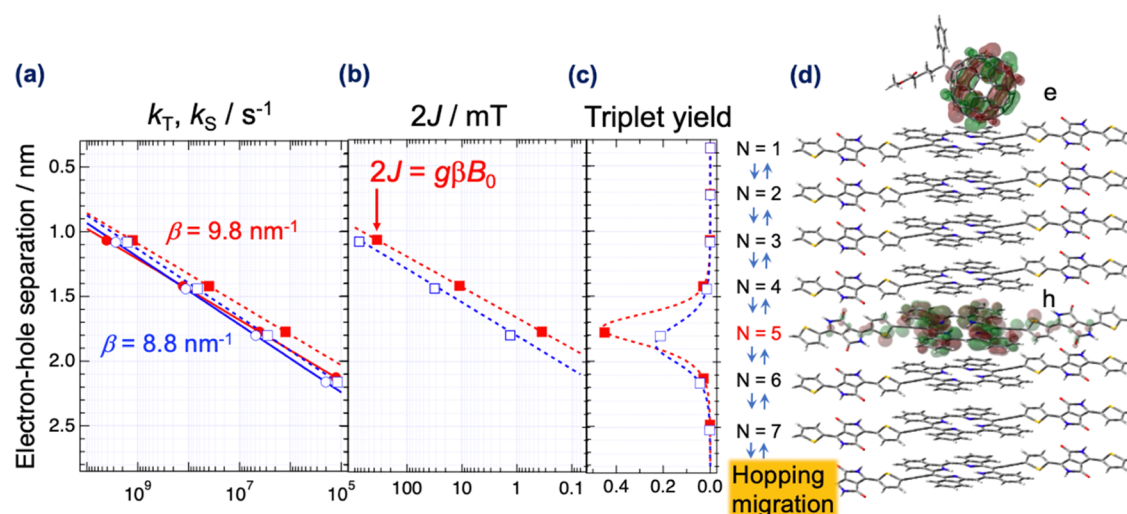
Figure 10. (a) Charge-recombination rate constants of $k_T(r)$ (solid lines and circles) and $k_S(r)$ (dashed lines and squares). β represents the attenuation factor in the r-dependence of electronic coupling. (b) $|S>-|0>$ electronic energy gap ($2J$). (c) Quantum yields of the triplet exciton products via $|S>-|0>$ conversion as a function of the separation distance. Plots in (c) are obtained by the density matrix formalism analysis applying (a) and (b) of the CS states of C4-DPP−H$_2$BP$^{+\bullet}$:PC$_{61}$BM$^{-\bullet}$ (red) and of C4-DPP−ZnBP$^{+\bullet}$:PC$_{61}$BM$^{-\bullet}$ (blue) at $t = 0.5$ μs. Initial singlet RP quantum yields are assumed to be 1 for all of the separations. (d) Corresponding geometry model of the separated geminate RP at $N = 5$ that causes selective triplet-recombination by the gate effect during the hole migrations.

Figure 9a. On the other hand, $r_{CC} > r_{\pi\pi}$ (=1.4 nm) denotes that the hole is situated in the disordered environment (Figure 9c) caused by zinc complexation.

Interestingly, the E/A signals became stronger at 0.5 μs than at 0.2 μs at the X-positions as shown by the red arrows in Figure 7a,b, while the outermost A/E polarized Z-transition intensities were unchanged by the delay times. These are explained by $|S>-|0>$ population relaxations[29,53] in the presence of J-couplings of 0.3 mT (0.5 mT) for the X directions with the relaxation time constant of $T_{23} = 0.7$ μs (3.0 μs) in C4-DPP−H$_2$BP:PC$_{61}$BM (C4-DPP−ZnBP:PC$_{61}$BM). This demonstrates that the J-couplings are fluctuating[54] to result in spin decoherences; the population of the eigenstate of $|b> = \cos \mu |S> + \sin \mu |0>$ becomes the same as that of $|c> = -\sin \mu |S> + \cos\mu |0>$, strongly indicating that the low-frequency phonon modes play a role in spin relaxation under the cryogenic condition,[27,29,55] as shown by the vertical blue arrows in Figure 9a.

DISCUSSION

Origins of Interfacial Charge-Separations in Nonpolymer Solar Cells

From the difference between the vertically separated electron−hole at $r_{CC} = 1.8$ nm in Figure 9 and the ^{1}CT* in Figure 8a (Figures S7b and S8b), it is evident that the electron−phonon (EP) coupling by the lattice motions between the π-stacking molecules induces separated charges, as shown by the vertical arrows in Figure 9a. Such a crystalline feature with the distance of $d = 0.35$ nm between the donor molecules is confirmed by the 2D-GIWAXD of the blend materials (Figure 3d), showing the face-on structures.

The present fluctuations are very consistent with the vibronic roles on the charge-dissociation from the ^{1}CT* state: the entropy enhancement occurs via the EP coupling between the orbital distribution and the low-frequency vibrations, overcoming the electrostatic stabilization in the ^{1}CT* state at the efficient electron−hole dissociation.[28,34,38]

Furthermore, quicker signal decays for the Y and Z-transitions than the decay at the X position are observed at delay times longer than 1 μs in Figure 7a,b. This is explained by the anisotropy in the spin−lattice relaxations in the triplet excitons as shown by the fitting lines with $T_{1X} = 6.0$ μs, $T_{1Y} = 0.5$ μs, and $T_{1Z} = 0.7$ μs, and thus, the combinations of (T_{23}, T_{1X}, T_{1Y}, T_{1Z}) are obtained from the delay time-dependences of the triplet EPR spectrum shapes for $t \geq 0.5$ μs in Figure 7. Such quick anisotropic relaxation is distinguished from the anisotropic T$_1$-S$_0$ intersystem crossing on eq S24,[56,57] indicating that the subtle fluctuations between the Y and Z principal axes are due to disordered rotational librations (red arrow at the X axis of Figure 9a) about the short axis (X) in the crystalline regions. This well coincides with the J-modulation to cause $|S>-|0>$ spin decoherence and thus is again consistent with the hole-dissociation mechanism via EP couplings. The present hole-dissociation mechanism via the phonon is clearly distinguished from the hot exciton dissociation[38,58] reported in polymer solar cells, in which the high-frequency vibration modes are involved in intrachain charge-dissociation. Control of the phonon effect is thus crucial for achieving high-performance nonpolymer solar cells utilizing small organic molecules. In addition, the present collective phonon's role is very consistent with $k_{CS} > 1$ ps^{-1} in Figure 8a, which is quicker than the exciton-diffusions. This is also supported by the ultrafast carrier dynamics studied by terahertz spectroscopy.[18,59]

Gating of Triplet Charge-Recombination from Heterogeneous CS States

To understand the uniqueness of the reported set of fitting parameters (Table 2 and Figure 9) for the heterogeneities in J, we examined whether a gating to capture the specific RP occurs in the triplet exciton products. We first performed calculations of the D−A separation distance (r) dependences of triplet and singlet charge-recombination rate constants $k_T(r)$ and $k_S(r)$ from the estimated electronic coupling of $V(r) = V_0 \exp(-\beta \, (r - d)/2)$ using the Marcus−Levich−Jortner theory (Figure 10a)[60]

$$k_{\mathrm{S,T}}(r) = \frac{2\pi}{h} \frac{|V(r)|^2}{\sqrt{4\pi\lambda_s k_{\mathrm{B}}T}} \sum_j FC_j$$

$$\exp\left\{-\frac{(\lambda_s + \Delta G_{\mathrm{S0,T}} + jh\nu_{\mathrm{vib}})^2}{4\lambda_s k_{\mathrm{B}}T}\right\} \tag{1}$$

with $FC_j = \exp(-S)S^j/j!$, where $S = \lambda_{\mathrm{V}}/h\nu_{\mathrm{vib}}$ with $j = 0,1,2,\cdots$. Here, λ_{V} and ν_{vib} represent the intramolecular reorganization energy and the vibration frequency, respectively. λ_{S} represents the solvent reorganization energy determined by the BHJ environment with the low-frequency response. The total reorganization energy (λ) is obtained by $\lambda = \lambda_{\mathrm{V}} + \lambda_{\mathrm{S}}$. Accordingly, the |S>-|0> energy gap $2J(r)$ is also computed using the configuration interaction model (Figure 10b), as follows[61]

$$2J(r) = -|V(r)|^2/\Delta E_{\mathrm{T}} + |V(r)|^2/\Delta E_{\mathrm{S}} \tag{2}$$

where ΔE_{T} and ΔE_{S} represent vertical energy gaps (expressed by $\Delta E_{\mathrm{S,T}} = -\Delta G_{\mathrm{S0,T}} - \lambda$, where $\Delta G_{\mathrm{S0,T}}$ and λ are corresponding driving forces and reorganization energies for the singlet and triplet-recombination processes, respectively). $\Delta G_{\mathrm{S0}} = -1.63$ and -1.44 eV are applied for the C4-DPP−H$_2$BP$^{+\bullet}$:PC$_{61}$BM$^{-\bullet}$ and C4-DPP−ZnBP$^{+\bullet}$:PC$_{61}$BM$^{-\bullet}$ systems, respectively, and are assumed to be r-independent. From the triplet state energies ($E_{\mathrm{T}} = 1.33$ eV and 1.36 eV),[62] $\Delta G_{\mathrm{T}} = \Delta G_{\mathrm{S0}} + E_{\mathrm{T}} = -0.30$ and -0.08 eV are applied for the triplet-recombination in the C4-DPP−H$_2$BP$^{+\bullet}$:PC$_{61}$BM$^{-\bullet}$ and C4-DPP−ZnBP$^{+\bullet}$:PC$_{61}$BM$^{-\bullet}$ systems, respectively. $\lambda_{\mathrm{S}} = 0.20$ eV, $\lambda_{\mathrm{V,T}} = 0.70$ eV, and $\lambda_{\mathrm{V,S0}} = 0.65$ eV are applied for the C4-DPP−H$_2$BP$^{+\bullet}$:PC$_{61}$BM$^{-\bullet}$ system with $\nu_{\mathrm{vib}} = 710$ cm^{-1}. In C4-DPP−ZnBP$^{+\bullet}$:PC$_{61}$BM$^{-\bullet}$, $\lambda_{\mathrm{S,T}} = 0.16$ eV, $\lambda_{\mathrm{S,S0}} = 0.23$ eV, $\lambda_{\mathrm{V,T}} = 0.39$ eV, and $\lambda_{\mathrm{V,S0}} = 0.46$ eV are applied with $\nu_{\mathrm{vib}} = 710$ cm^{-1}. These energies are parameterized to reproduce the values of k_{T}, k_{S}, and J in Table 2 at $r = 1.8$ nm. However, the other parameter sets are plausible to explain the experimental results because of several uncertain reorganization parameters incorporated in eqs 1 and 2. Validities of the above λ values are demonstrated in the following subsection.

When $\beta = 9.8$ nm^{-1} (8.8 nm^{-1} in blue lines for C4-DPP−ZnBP$^{+\bullet}$ − PC$_{61}$BM$^{-\bullet}$, Figure 10) is employed in $V(r)$ with $V_0 = 660$ cm^{-1} (610 cm^{-1}) at $d = 0.35$ nm, $10^6 < k_{\mathrm{S,T}} < 10^7$ (s^{-1}) is obtained for $r = 1.8$ nm satisfying $k_{\mathrm{T}} > k_{\mathrm{S}}$, which is consistent with the rises in the triplet products, as the rate-determining processes of the gating when hole migrations are quick. The V_0 values are compatible with the electronic coupling reported in the CT complexes by Farid and co-workers.[63] We next computed the quantum yield of the excited triplet state at 0.5 μs in eq S2 (Figure 10c) for the exciton product by the density matrix formalism analysis applying Figure 10a,b under the assumption that the singlet RPs are evenly distributed for all of the D−A separations. Despite this simple assumption, Figure 10c demonstrates the gate effect of the specific RPs at 1.8 nm from the widths of the peaks. Furthermore, charge-separation distances are thought to be stepwise when the hole is localized in a DPP−BP molecule as shown in Figure 9. Thus, from the crystalline structure with $d = 0.357$ and 0.361 nm in C4-DPP−H$_2$BP and in C4-DPP−ZnBP, respectively, the triplet yields are plotted from the contact RP ($r = 0.35$ nm, $N = 1$) to the highly separated pairs ($r = 2.5$ nm, $N = 7$), as shown by the squares in Figure 10b,c. From the ordering of the π−π stacking, the electron−hole (e−h) separations at 1.8 nm are consistent with the separated pair of $N = 5$ exhibiting highest triplet yields in

Figure 10d. Overall, the uniqueness of the geometries originates from the gating that causes the capture of the weakly coupled RP at $r = 1.8$ nm of $N = 5$. The residual separated RPs that escape from this capture are observed at the center field positions in Figures 7 and S16 and S17. More details on the recombination dynamics are described in Figure S22.

Connection between Cell Performance and Microscopic Structure

From the charge-separation dominantly occurring from the ^{1}CT* state, we estimated voltage losses (Table 1) from ^{1}CT* levels using the E_{CT} values determined by the CT emissions, considering that the band gaps are almost degenerated with the ^{1}CT* energies (Figures 4 and S7), as follows[19,24]

$$\Delta V_{\mathrm{OC}} = E_{\mathrm{CT}}/q - V_{\mathrm{OC}} \tag{3}$$

where q represents the elementary charge. The voltage loss in eq 3 includes the radiative loss (ΔV_{r}) and the nonradiative loss (ΔV_{nr}).[19] We characterized ultrafast efficient charge-separation events with $k_{\mathrm{CS}} > 1$ ps^{-1} (Figure 6c,d), which is much larger than the rate of the radiative process, and obtained the nanosecond triplet-recombination process (Figure 8c). It is thus anticipated that the nonradiative process largely affects ΔV_{OC} in Table 1.

It is challenging to discuss whether the present distant CS states trapped at 80 K correlate with the device performance. However, the present vertically separated CS geometries with $(\theta, \phi) = (20, 0°)$ strongly denote that the phonon-assisted hole-dissociations occur only via the one-dimensional (1D) carrier-conductions[64] and should be a characteristic of the nonpolymer solar cells, as opposed to the three-dimensional (3D) routes for carrier dissociations found in polymer solar cells at cryogenic conditions.[28,31] This difference indicates that the present 1D carrier motions can readily cause recombination loss[64] from the highly separated e−h pairs via the assistance of phonons because backward e−h encounters are more plausible to occur than in the 3D environments. This well supports the time-resolved photocurrent observations that demonstrated the nanosecond carrier recombination dynamics by the first- and second-order processes.[18] From Table 1, ΔV_{OC} is lower in the C4-DPP−ZnBP:PC$_{61}$BM device than that in C4-DPP−H$_2$BP:PC$_{61}$BM although the PCEs and the EQEs are similar. To examine the correlation between the T_0-recombination effects and OSC performances, we performed the mapping of the Φ_{T_0} populations at 0.2 μs for C4-DPP−ZnBP:PC$_{61}$BM (Figure 9d) from Table 2. Although the mapping resembles the color maps of Figures 9b and S23, the Φ_{T_0} values are much smaller in C4-DPP−ZnBP:PC$_{61}$BM. This is explained by the prohibited spin-conversion in the presence of the stronger J-coupling to increase ΔE_{ST} in C4-DPP−ZnBP:PC$_{61}$BM (Table 2) with the reduced J-modulation by the longer T_{23} (=3 μs). This indicates that the distant CS plays a role in improving the voltage loss $(\Delta V_{\mathrm{OC}} = 0.86$ V) in Table 1, particularly when the detrapped charges are undergoing 1D diffusion during device operations. The stronger sharp CS-state signal around 340 mT in Figure 7b strongly supports the lower ΔV_{OC} (=0.86 V) in the zinc substituent system compared to $\Delta V_{\mathrm{OC}} = 1.03$ V in free-base porphyrin due to suppression of nonradiative recombination.[23] The stronger J of the CS state in Figure 9c is from the weaker attenuation in β to strengthen the orbital overlap by C4-DPP−ZnBP$^{+\bullet}$ than by C4-DPP−H$_2$BP$^{+\bullet}$

due to the smaller reorganization barrier, as detailed in the following subsection.

Phonon Engineering for Cell Performance

In addition to T_0 recombination, the T_+ generation in Figure 8 should be problematic although the spin–orbit coupling-induced recombination (SOC-CR in Figure 8) is absent. The emissive ESP in Figure 7a is explained by introducing the T_+ population with the quantum yield (Φ_+) of 0.10. When the separated singlet RP ($|S\rangle$) is generated at $N = 5$ (Figure 10d) via the hopping migration mediated by the phonon, the $|+\rangle$ in the RP can also be populated via the quick migration competing with $k_T(r)$. Based on this, it is notable that $2J$ (=350 mT) in the separated pair at $N = 3$ in Figure 10b is almost equal to the Zeeman energy (=340 mT) at the X-band for $\beta = 9.8$ nm^{-1}, as indicated by the red arrow in Figure 10b at 1.1 nm. This denotes that $|S\rangle$-$|+\rangle$ conversion and subsequent dissociation in $|+\rangle$ are possible during repetitive hole motions. The emissive spin polarization in the center region (Figure 7a) is the result of the dissociation after the $|S\rangle$-$|+\rangle$ conversion. This is very reasonable because such an emissive spin polarization is absent in the Q-band TREPR measurement (Figure S20); no $|S\rangle$-$|+\rangle$ resonance occurs in the high-field (1220 mT) experiment during the stepwise hole motions, resulting in the absence of emissive polarization also for the triplet product.

The reorganization energies ($\lambda = 0.89$ eV in C4-DPP–H$_2$BP$^{+\bullet}$:PC$_{61}$BM$^{-\bullet}$ and 0.55 eV in C4-DPP–ZnBP$^{+\bullet}$:PC$_{61}$BM$^{-\bullet}$) are required to self-consistently explain the gating effects for the different D:A systems and coincide with the broad ^{1}CT* emission bands in Figure 4. In addition, a recent study on the hole transfer reaction in copper-phthalocyanine crystalline films demonstrated that the reorganization energy for the intermolecular hopping is 0.93 eV.[65] These strong reorganizations imply that the hole is not delocalized and undergoes quick hopping dissociation assisted by the phonon. As for $V(r) = V_0 \exp(-\beta(r - d)/2)$ of the separated RPs, McConnell's electron-tunneling model is applicable in β, as follows[66]

$$\beta = (2/d)\ln(\Delta E/|V_{\pi\pi}|) \tag{4}$$

where ΔE and $V_{\pi\pi}$ represent tunneling barrier height of the CS state for the hole conduction and transfer integral between the π–π stacking molecules, respectively. From this, $\Delta E = 0.48$ eV (0.37 eV) and $|V_{\pi\pi}| = 660$ cm^{-1} (610 cm^{-1}) are estimated to explain $\beta = 9.8$ nm^{-1} (8.8 nm^{-1}) in Figure 10a. $|V_0| = |V_{\pi\pi}| = 660$ cm^{-1} at $d = 0.35$ nm indicates that the strong transfer integral by the π–π stacking is enhanced by the nuclear motions between the molecules, according to the non-Condon effect.[38] From $\Delta E = 0.48$ eV (0.37 eV) in eq 4, $2\Delta E \approx \lambda$ is the manifestation that the electronic tunneling is determined by the reorganization barrier height, as described by Beratan and co-workers.[67] This demonstrates the validity of the hopping migrations causing the gate effect from the separated RPs at $N = 5$. Overall, because the reorganization barrier is much larger than the transfer integral ($V_{\pi\pi}$) in the present systems, the localized holes by the one C4-DPP–BP$^{+\bullet}$ unit compose the separated RPs (Figure 10d) and are distinguished from the delocalized hole[50,68] in the CS states of the polymer solar cells that exhibit weaker electronic attenuations ($\beta < 2$ nm^{-1}).[10,28] This is very consistent with applications of the point dipole approximation for the separated radicals to determine $r_{CC} = 1.8$ nm.

We thus propose that the separated pairs at $N \geq 3$ are produced through the vertical phonon mode causing the J-modulation,[69] as shown in Figure 9a; too much ordered lattice motions[39] may induce repetitive 1D-backscattering hole motions coupled with the phonon from the geminately separated e–h pairs in the nonpolymer solar cell, as shown in Figure 8. The nongeminate process[18,25,70] is excluded to account for the present spin polarization, as follows. If the nongeminate recombination from the spin statistical distribution by the e–h encounter was the source of the spin polarization, T_+ and T_- populations should be preferential to cause a totally different spin polarization from the present result for the positive D_T because the $|S\rangle$-$|0\rangle$ mixing should inhibit the T_0 population when $k_S < k_T$. In the C4-DPP-H$_2$BP:PCBM solar cell, the geminate recombination effect was dominant in the transient photocurrent decay profile, while the nongeminate recombination was negligible in the submicrosecond regions.[18] Given that ΔV_{OC} is larger in the C4-DPP-H$_2$BP:PCBM solar cell than in the C4-DPP-ZnBP:PCBM system, the impact of the nongeminate process is not the reason for the ΔV_{OC} difference in Table 1, although the nongeminate processes might influence the voltages themselves.

From Table 2, the singlet–triplet dephasing time (T_{23}) is longer in the C4-DPP–ZnBP:PC$_{61}$BM system than in the free-base system that exhibited the T_+ population, indicating that the ordered acoustic motions[39] in the donor domain are insufficient to produce the separated pairs at $N = 3$. This elongation in T_{23} is rationalized by the slightly longer d-spacings for the π–π stacking (3.61 Å) in the Zn-substituted systems than in the free-base systems in Figure 3, resulting in the weaker π–π lattice interactions by introducing Zn^{2+} to the BP moieties. The present weakened phonon motions are thus explained by the slight geometrical disorders for $N \geq 5$ in the C4-DPP–ZnBP conformations in Figure 10d, reducing the mean crystalline size to $r_{\pi\pi} = 1.4$ nm derived from the broader diffraction peaks in the red lines of Figure 3b,d. Overall, the improved cell performances in the ZnBP system originate from regulations of the phonon associated with the disordered π-stackings to ensure charge-dissociation by entropy. It is concluded that, while disordered motions in Figure 9c are essential to enhance the entropy for charge dissociations,[38] too much ordered crystallinity causes the backscattering acoustic phonon as a wrong phonon to reduce the OSC performances, resulting in the loss of V_{OC}.

■ CONCLUSIONS

We comprehensively investigated the origins of photocarrier generation and nonradiative deactivation using various spectroscopic tools including the microscopic spatial and orientational imaging methods to elucidate details of the underlying dynamics of nonpolymer solar cells. The ^{1}CT* states (Figure 8a), whose energies are 1.46 eV (C4-DPP–ZnBP:PC$_{61}$BM) and 1.65 eV (C4-DPP–H$_2$BP:PC$_{61}$BM), are generated via picosecond exciton-diffusions and cause efficient photocarriers by quick charge-separations. However, the voltage loss of $\Delta V_{OC} = 0.86$ V in C4-DPP–ZnBP:PC$_{61}$BM OSC is revealed to be lower than that of $\Delta V_{OC} = 1.03$ V in free-base porphyrin system.

From the TREPR analysis, we have obtained details of the geometries of the distant CS state with $r_{CC} = 1.8$ nm causing voltage losses by quantum yield imaging maps of the T_0-sublevel recombination using electron spin polarizations of the

triplet excitons (Figure 9). From the analysis of the distance dependence of the anisotropic recombination dynamics, we clarified the gating effect for T_0-recombinations capturing the separated geminate RP ($N = 5$) generated by hopping hole migration from the ^{1}CT* states. The EP coupling originating from the crystalline packings was revealed to play a role in producing the CS states from ^{1}CT* by the lattice librations between the π-stacking molecules in the donor domains, as shown by the vertical arrows in Figure 9a. However, such distant CS states cause problematic losses in the voltage due to nanosecond triplet-recombination processes during the 1D-backscattering charge motions in the ordered interface regions. Importantly, such an acoustic phonon can be regulated by controlling the d-spacings when employing the ZnBP donor to ensure highly separated CS-state generations that lived more than 10 μs. Introducing a slight disorder to weaken the $\pi-\pi$ lattice interactions is a key to enhancing the entropy (or density of state) for the charge-dissociation processes reducing the radiative and nonradiative voltage losses for future development of small-molecule solar cells that employ 1D dissociative charge-conductions, while such ordered phonons can be useful for organic light-emitting diodes to enhance the radiative recombination from separated e−h pairs.[38]

■ ASSOCIATED CONTENT

Ⓢ Supporting Information

The Supporting Information is available free of charge at https://pubs.acs.org/doi/10.1021/acsphyschemau.2c00049.

> Materials, characterizations of OSCs, thermogravimetric analysis, photoelectron spectra, fluorescence spectroscopy, AFM images, molecular orbital calculations, transient absorption spectroscopy, TREPR spectroscopy, theoretical analysis of the EPR data including the quantum yield imaging map of the CS states (PDF)

■ AUTHOR INFORMATION

Corresponding Authors

Sadahiro Masuo − *Department of Applied Chemistry for Environment, Kwansei Gakuin University, Sanda, Hyogo 669-1337, Japan;* ● orcid.org/0000-0003-4828-5968; Email: masuo@kwansei.ac.jp

Kaoru Ohta − *Molecular Photoscience Research Center, Kobe University, Nada, Kobe 657-8501, Japan;* ● orcid.org/0000-0002-4687-7989; Email: kohta@kobe-u.ac.jp

Hiroko Yamada − *Division of Materials Science, Graduate School of Science and Technology, Nara Institute of Science and Technology, Ikoma, Nara 630-0192, Japan;* ● orcid.org/0000-0002-2138-5902; Email: hyamada@ms.naist.jp

Yasuhiro Kobori − *Department of Chemistry, Graduate School of Science, Kobe University, Nada, Kobe 657-8501, Japan; Molecular Photoscience Research Center, Kobe University, Nada, Kobe 657-8501, Japan;* ● orcid.org/0000-0001-8370-9362; Email: ykobori@kitty.kobe-u.ac.jp

Authors

Takaaki Nagatomo − *Department of Chemistry, Graduate School of Science, Kobe University, Nada, Kobe 657-8501, Japan*

Ajendra K. Vats − *Division of Materials Science, Graduate School of Science and Technology, Nara Institute of Science and Technology, Ikoma, Nara 630-0192, Japan*

Kyohei Matsuo − *Division of Materials Science, Graduate School of Science and Technology, Nara Institute of Science and Technology, Ikoma, Nara 630-0192, Japan;* ● orcid.org/0000-0002-2472-9459

Shinya Oyama − *Department of Chemistry, Graduate School of Science, Kobe University, Nada, Kobe 657-8501, Japan*

Naoya Okamoto − *Division of Materials Science, Graduate School of Science and Technology, Nara Institute of Science and Technology, Ikoma, Nara 630-0192, Japan*

Mitsuharu Suzuki − *Division of Applied Chemistry, Graduate School of Engineering, Osaka University, Suita, Osaka 565-0871, Japan;* ● orcid.org/0000-0002-0121-2561

Tomoyuki Koganezawa − *Japan Synchrotron Radiation Research Institute (JASRI), Sayo, Hyogo 679-5198, Japan*

Masaaki Fuki − *Department of Chemistry, Graduate School of Science, Kobe University, Nada, Kobe 657-8501, Japan; Molecular Photoscience Research Center, Kobe University, Nada, Kobe 657-8501, Japan*

Complete contact information is available at:
https://pubs.acs.org/10.1021/acsphyschemau.2c00049

Author Contributions

CRediT: **Takaaki Nagatomo** conceptualization (supporting), data curation (equal), formal analysis (supporting), funding acquisition (supporting), investigation (equal), methodology (equal), project administration (supporting), resources (supporting), software (supporting), supervision (supporting), validation (equal), visualization (supporting), writing-original draft (supporting), writing-review & editing (supporting); **Ajendra K Vats** data curation (equal), formal analysis (equal), investigation (equal), methodology (equal), validation (equal); **Kyohei Matsuo** data curation (equal), investigation (equal), methodology (equal), validation (equal), writing-original draft (equal); **Shinya Oyama** data curation (supporting), formal analysis (supporting), investigation (supporting), methodology (supporting); **Naoya Okamoto** data curation (supporting), investigation (supporting), methodology (supporting); **Mitsuharu Suzuki** data curation (equal), formal analysis (equal), investigation (equal), methodology (equal), resources (equal), supervision (supporting), writing-original draft (supporting), writing-review & editing (supporting); **Tomoyuki Koganezawa** data curation (equal), formal analysis (equal), investigation (equal), methodology (equal), resources (equal), software (equal), validation (equal); **Masaaki Fuki** data curation (equal), formal analysis (equal), investigation (supporting), methodology (supporting), software (equal), writing-original draft (supporting); **Sadahiro Masuo** data curation (equal), formal analysis (equal), investigation (equal), methodology (equal), project administration (equal), resources (equal), validation (equal), visualization (equal), writing-original draft (equal), writing-review & editing (equal); **Kaoru Ohta** data curation (equal), formal analysis (equal), investigation (equal), methodology (equal), resources (equal), writing-original draft (equal), writing-review & editing (equal); **Hiroko Yamada** conceptualization (equal), funding acquisition (equal), investigation (equal), methodology (equal), project administration (equal), resources (equal), supervision (equal), validation (equal), visualization (equal), writing-original draft (equal), writing-review & editing (equal); **Yasuhiro Kobori** conceptualization (lead), data curation (lead), formal analysis (lead), funding acquisition (lead), investigation (lead), methodology (equal), project administration (lead), resources (equal),

REFERENCES

(1) Liu, F.; Zhou, L.; Liu, W.; Zhou, Z.; Yue, Q.; Zheng, W.; Sun, R.; Liu, W.; Xu, S.; Fan, H.; Feng, L.; Yi, Y.; Zhang, W.; Zhu, X. Organic Solar Cells with 18% Efficiency Enabled by an Alloy Acceptor: A Two-in-One Strategy. *Adv. Mater.* **2021**, *33*, No. 2100830.

(2) Wadsworth, A.; Moser, M.; Marks, A.; Little, M. S.; Gasparini, N.; Brabec, C. J.; Baran, D.; McCulloch, I. Critical review of the molecular design progress in non-fullerene electron acceptors towards commercially viable organic solar cells. *Chem. Soc. Rev.* **2019**, *48*, 1596−1625.

(3) Hou, J.; Inganäs, O.; Friend, R. H.; Gao, F. Organic solar cells based on non-fullerene acceptors. *Nat. Mater.* **2018**, *17*, 119−128.

(4) Yan, C.; Barlow, S.; Wang, Z.; Yan, H.; Jen, A. K. Y.; Marder, S. R.; Zhan, X. Non-fullerene acceptors for organic solar cells. *Nat. Rev. Mater.* **2018**, *3*, 18003.

(5) Lin, Y.; Nugraha, M. I.; Firdaus, Y.; Scaccabarozzi, A. D.; Aniés, F.; Emwas, A.-H.; Yengel, E.; Zheng, X.; Liu, J.; Wahyudi, W.; Yarali, E.; Faber, H.; Bakr, O. M.; Tsetseris, L.; Heeney, M.; Anthopoulos, T. D. A Simple n-Dopant Derived from Diquat Boosts the Efficiency of Organic Solar Cells to 18.3%. *ACS Energy Lett.* **2020**, *5*, 3663−3671.

(6) Lin, Y.; Firdaus, Y.; Isikgor, F. H.; Nugraha, M. I.; Yengel, E.; Harrison, G. T.; Hallani, R.; El-Labban, A.; Faber, H.; Ma, C.; Zheng, X.; Subbiah, A.; Howells, C. T.; Bakr, O. M.; McCulloch, I.; Wolf, S. D.; Tsetseris, L.; Anthopoulos, T. D. Self-Assembled Monolayer Enables Hole Transport Layer-Free Organic Solar Cells with 18% Efficiency and Improved Operational Stability. *ACS Energy Lett.* **2020**, *5*, 2935−2944.

(7) Guo, J. M.; Ohkita, H.; Benten, H.; Ito, S. Charge Generation and Recombination Dynamics in Poly(3-hexylthiophene)/Fullerene Blend Films with Different Regioregularities and Morphologies. *J. Am. Chem. Soc.* **2010**, *132*, 6154−6164.

(8) Tamai, Y.; Matsuura, Y.; Ohkita, H.; Benten, H.; Ito, S. One-Dimensional Singlet Exciton Diffusion in Poly(3-hexylthiophene) Crystalline Domains. *J. Phys. Chem. Lett.* **2014**, *5*, 399−403.

(9) Tamai, Y.; Ohkita, H.; Benten, H.; Ito, S. Exciton Diffusion in Conjugated Polymers: From Fundamental Understanding to Improvement in Photovoltaic Conversion Efficiency. *J. Phys. Chem. Lett.* **2015**, *6*, 3417−3428.

(10) Miura, T.; Aikawa, M.; Kobori, Y.; Time-Resolved, EPR. Study of Electron-Hole Dissociations Influenced by Alkyl Side Chains at the Photovoltaic Polyalkylthiophene:PCBM Interface. *J. Phys. Chem. Lett.* **2014**, *5*, 30−35.

(11) Giannini, S.; Carof, A.; Ellis, M.; Yang, H.; Ziogos, O. G.; Ghosh, S.; Blumberger, J. Quantum localization and delocalization of charge carriers in organic semiconducting crystals. *Nat. Commun.* **2019**, *10*, No. 3843.

(12) Wang, L.-M.; Li, Q.; Liu, S.; Cao, Z.; Cai, Y.-P.; Jiao, X.; Lai, H.; Xie, W.; Zhan, X.; Zhu, T. Quantitative Determination of the Vertical Segregation and Molecular Ordering of PBDB-T/ITIC Blend

(13) Films with Solvent Additives. *ACS Appl. Mater. Interfaces* **2020**, *12*, 24165−24173.

(13) Huang, Y.; Kramer, E. J.; Heeger, A. J.; Bazan, G. C. Bulk Heterojunction Solar Cells: Morphology and Performance Relationships. *Chem. Rev.* **2014**, *114*, 7006−7043.

(14) Matsuo, Y.; Sato, Y.; Niinomi, T.; Soga, I.; Tanaka, H.; Nakamura, E. Columnar Structure in Bulk Heterojunction in Solution-Processable Three-Layered p-i-n Organic Photovoltaic Devices Using Tetrabenzoporphyrin Precursor and Silylmethyl[60]-fullerene. *J. Am. Chem. Soc.* **2009**, *131*, 16048−16050.

(15) Schmidt-Mende, L.; Fechtenkötter, A.; Müllen, K.; Moons, E.; Friend, R. H.; MacKenzie, J. D. Self-Organized Discotic Liquid Crystals for High-Efficiency Organic Photovoltaics. *Science* **2001**, *293*, 1119−1122.

(16) Walker, B.; Kim, C.; Nguyen, T.-Q. Small Molecule Solution-Processed Bulk Heterojunction Solar Cells. *Chem. Mater.* **2011**, *23*, 470−482.

(17) Takahashi, K.; Kumagai, D.; Yamada, N.; Kuzuhara, D.; Yamaguchi, Y.; Aratani, N.; Koganezawa, T.; Koshika, S.; Yoshimoto, N.; Masuo, S.; Suzuki, M.; Nakayama, K.-i.; Yamada, H. Side-chain engineering in a thermal precursor approach for efficient photocurrent generation. *J. Mater. Chem. A* **2017**, *5*, 14003−14011.

(18) Kudo, N.; Uchida, K.; Ikoma, T.; Takahashi, K.; Kuzuhara, D.; Suzuki, M.; Yamada, H.; Kumagai, D.; Yamaguchi, Y.; Nakayama, K.-I. Transient Photocurrent Elucidating Carrier Dynamics and Potential of Bulk Heterojunction Solar Cells Fabricated by Thermal Precursor Approach. *Solar RRL* **2018**, *2*, No. 1700234.

(19) Han, G.; Yi, Y. Local Excitation/Charge-Transfer Hybridization Simultaneously Promotes Charge Generation and Reduces Nonradiative Voltage Loss in Nonfullerene Organic Solar Cells. *J. Phys. Chem. Lett.* **2019**, *10*, 2911−2918.

(20) Qian, D.; Zheng, Z.; Yao, H.; Tress, W.; Hopper, T. R.; Chen, S.; Li, S.; Liu, J.; Chen, S.; Zhang, J.; Liu, X.-K.; Gao, B.; Ouyang, L.; Jin, Y.; Pozina, G.; Buyanova, I. A.; Chen, W. M.; Inganäs, O.; Coropceanu, V.; Bredas, J.-L.; Yan, H.; Hou, J.; Zhang, F.; Bakulin, A. A.; Gao, F. Design rules for minimizing voltage losses in high-efficiency organic solar cells. *Nat. Mater.* **2018**, *17*, 703−709.

(21) Chen, X.-K.; Qian, D.; Wang, Y.; Kirchartz, T.; Tress, W.; Yao, H.; Yuan, J.; Hülsbeck, M.; Zhang, M.; Zou, Y.; Sun, Y.; Li, Y.; Hou, J.; Inganäs, O.; Coropceanu, V.; Bredas, J.-L.; Gao, F. A unified description of non-radiative voltage losses in organic solar cells. *Nat. Energy* **2021**, *6*, 799−806.

(22) Kang, H.; Zhang, X.; Xu, X.; Li, Y.; Li, S.; Cheng, Q.; Huang, L.; Jing, Y.; Zhou, H.; Ma, Z.; Zhang, Y. Strongly Reduced Non-Radiative Voltage Losses in Organic Solar Cells Prepared with Sequential Film Deposition. *J. Phys. Chem. Lett.* **2021**, *12*, 10663−10670.

(23) Eisner, F. D.; Azzouzi, M.; Fei, Z.; Hou, X.; Anthopoulos, T. D.; Dennis, T. J. S.; Heeney, M.; Nelson, J. Hybridization of Local Exciton and Charge-Transfer States Reduces Nonradiative Voltage Losses in Organic Solar Cells. *J. Am. Chem. Soc.* **2019**, *141*, 6362−6374.

(24) Saito, T.; Natsuda, S.-i.; Imakita, K.; Tamai, Y.; Ohkita, H. Role of Energy Offset in Nonradiative Voltage Loss in Organic Solar Cells. *Solar RRL* **2020**, *4*, No. 2000255.

(25) Gillett, A. J.; Privitera, A.; Dilmurat, R.; Karki, A.; Qian, D.; Pershin, A.; Londi, G.; Myers, W. K.; Lee, J.; Yuan, J.; Ko, S.-J.; Riede, M. K.; Gao, F.; Bazan, G. C.; Rao, A.; Nguyen, T.-Q.; Beljonne, D.; Friend, R. H. The role of charge recombination to triplet excitons in organic solar cells. *Nature* **2021**, *597*, 666−671.

(26) Zeidan, T. A.; Carmieli, R.; Kelley, R. F.; Wilson, T. M.; Lewis, F. D.; Wasielewski, M. R. Charge-Transfer and Spin Dynamics in DNA Hairpin Conjugates with Perylenediimide as a Base-Pair Surrogate. *J. Am. Chem. Soc.* **2008**, *130*, 13945−13955.

(27) Hamada, M.; Iwata, T.; Fuki, M.; Kandori, H.; Weber, S.; Kobori, Y. Orientations and water dynamics of photoinduced secondary charge-separated states for magnetoreception by cryptochrome. *Commun. Chem.* **2021**, *4*, 141.

(28) Kobori, Y.; Ako, T.; Oyama, S.; Tachikawa, T.; Marumoto, K. Transient Electron Spin Polarization Imaging of Heterogeneous Charge-Separation Geometries at Bulk-Heterojunction Interfaces in Organic Solar Cells. *J. Phys. Chem. C* **2019**, *123*, 13472−13481.

(29) Hasegawa, M.; Nagashima, H.; Minobe, R.; Tachikawa, T.; Mino, H.; Kobori, Y. Regulated Electron Tunneling of Photoinduced Primary Charge-Separated State in the Photosystem II Reaction Center. *J. Phys. Chem. Lett.* **2017**, *8*, 1179−1184.

(30) Harvey, S. M.; Wasielewski, M. R. Photogenerated Spin-Correlated Radical Pairs: From Photosynthetic Energy Transduction to Quantum Information Science. *J. Am. Chem. Soc.* **2021**, *143*, 15508−15529.

(31) Jinnai, S.; Murayama, K.; Nagai, K.; Mineshita, M.; Kato, K.; Muraoka, A.; Yamakata, A.; Saeki, A.; Kobori, Y.; Ie, Y. Effects of the rigid and sterically bulky structure of non-fused nonfullerene acceptors on transient photon-to-current dynamics. *J. Mater. Chem. A* **2022**, *10*, 20035−20047.

(32) Lukina, E. A.; Popov, A. A.; Uvarov, M. N.; Kulik, L. V. Out-of-Phase Electron Spin Echo Studies of Light-Induced Charge-Transfer States in P3HT/PCBM Composite. *J. Phys. Chem. B* **2015**, *119*, 13543−13548.

(33) Kobori, Y.; Ponomarenko, N.; Norris, J. R. Time-Resolved Electron Paramagnetic Resonance Study on Cofactor Geometries and Electronic Couplings after Primary Charge Separations in the Photosynthetic Reaction Center. *J. Phys. Chem. C* **2015**, *119*, 8078−8088.

(34) Miura, T.; Tao, R.; Shibata, S.; Umeyama, T.; Tachikawa, T.; Imahori, H.; Kobori, Y. Geometries, Electronic Couplings, and Hole Dissociation Dynamics of Photoinduced Electron−Hole Pairs in Polyhexylthiophene−Fullerene Dyads Rigidly Linked by Oligophenylenes. *J. Am. Chem. Soc.* **2016**, *138*, 5879−5885.

(35) Vukmirović, N.; Wang, L.-W. Carrier hopping in disordered semiconducting polymers: How accurate is the Miller−Abrahams model? *Appl. Phys. Lett.* **2010**, *97*, No. 043305.

(36) Cheung, D. L.; McMahon, D. P.; Troisi, A. Computational Study of the Structure and Charge-Transfer Parameters in Low-Molecular-Mass P3HT. *J. Phys. Chem. B* **2009**, *113*, 9393−9401.

(37) Krinichnyi, V. I.; Yudanova, E. I.; Spitsina, N. G. Light-Induced Electron Paramagnetic Resonance Study of Poly(3-alkylthiophene)/Fullerene Composites. *J. Phys. Chem. C* **2010**, *114*, 16756−16766.

(38) Imahori, H.; Kobori, Y.; Kaji, H. Manipulation of Charge-Transfer States by Molecular Design: Perspective from "Dynamic Exciton". *Acc. Mater. Res.* **2021**, *2*, 501−514.

(39) Martiradonna, L. Riddles in perovskite research. *Nat. Mater.* **2018**, *17*, 377.

(40) Smilgies, D. M. Scherrer grain-size analysis adapted to grazing-incidence scattering with area detectors. *J. Appl. Crystallogr.* **2009**, *42*, 1030−1034.

(41) Rivnay, J.; Mannsfeld, S. C. B.; Miller, C. E.; Salleo, A.; Toney, M. F. Quantitative Determination of Organic Semiconductor Microstructure from the Molecular to Device Scale. *Chem. Rev.* **2012**, *112*, 5488−5519.

(42) Huang, T.-Y.; Yan, H.; Abdelsamie, M.; Savikhin, V.; Schneider, S. A.; Ran, N. A.; Nguyen, T.-Q.; Bazan, G. C.; Toney, M. F. Fullerene derivative induced morphology of bulk heterojunction blends: PIPCP:PC61BM. *RSC Adv.* **2019**, *9*, 4106−4112.

(43) Imahori, H.; Tkachenko, N. V.; Vehmanen, V.; Tamaki, K.; Lemmetyinen, H.; Sakata, Y.; Fukuzumi, S. An Extremely Small Reorganization Energy of Electron Transfer in Porphyrin−Fullerene Dyad. *J. Phys. Chem. A* **2001**, *105*, 1750−1756.

(44) Keiderling, C.; Dimitrov, S.; Durrant, J. R. Exciton and Charge Generation in PC60BM Thin Films. *J. Phys. Chem. C* **2017**, *121*, 14470−14475.

(45) Dance, Z. E. X.; Mi, Q. X.; McCamant, D. W.; Ahrens, M. J.; Ratner, M. A.; Wasielewski, M. R. Time-resolved EPR studies of photogenerated radical ion pairs separated by p-phenylene oligomers and of triplet states resulting from charge recombination. *J. Phys. Chem. B* **2006**, *110*, 25163−25173.

(46) Thurnauer, M. C.; Katz, J. J.; Norris, J. R. The triplet state in bacterial photosynthesis: Possible mechanisms of the primary photoact. *Proc. Natl. Acad. Sci. U.S.A.* **1975**, *72*, 3270−3274.

(47) Salvadori, E.; Luke, N.; Shaikh, J.; Leventis, A.; Bronstein, H.; Kay, C. W. M.; Clarke, T. M. Ultra-fast spin-mixing in a diketopyrrolopyrrole monomer/fullerene blend charge transfer state. *J. Mater. Chem. A* **2017**, *5*, 24335−24343.

(48) Kay, C. W. M. The Electronic Structure of the Photoexcited Triplet State of Free-Base (Tetraphenyl)porphyrin by Time-Resolved Electron−Nuclear Double Resonance and Density Functional Theory. *J. Am. Chem. Soc.* **2003**, *125*, 13861−13867.

(49) Tait, C. E.; Neuhaus, P.; Anderson, H. L.; Timmel, C. R. Triplet State Delocalization in a Conjugated Porphyrin Dimer Probed by Transient Electron Paramagnetic Resonance Techniques. *J. Am. Chem. Soc.* **2015**, *137*, 6670−6679.

(50) Niklas, J.; Mardis, K. L.; Banks, B. P.; Grooms, G. M.; Sperlich, A.; Dyakonov, V.; Beaupre, S.; Leclerc, M.; Xu, T.; Yu, L. P.; Poluektov, O. G. Highly-efficient charge separation and polaron delocalization in polymer-fullerene bulk-heterojunctions: a comparative multi-frequency EPR and DFT study. *Phys. Chem. Chem. Phys.* **2013**, *15*, 9562−9574.

(51) Osintsev, A.; Popov, A.; Fuhs, M.; Möbius, K. Spin dynamics in strongly coupled spin-correlated radical pairs: Stochastic modulation of the exchange interaction and ST−1 mixing in different magnetic fields. *Appl. Magn. Reson.* **2001**, *20*, 111−135.

(52) Till, U.; Klenina, I. B.; Proskuryakov, I. I.; Hoff, A. J.; Hore, P. J. Recombination Dynamics and EPR Spectra of the Primary Radical Pair in Bacterila Photosynthetic Reaction Centers with Blocked Electron Transfer to the Primary Acceptor. *J. Phys. Chem. B* **1997**, *101*, 10939−10948.

(53) Fukuju, T.; Yashiro, H.; Maeda, K.; Murai, H.; Azumi, T. Singlet-Born SCRP Observed in the Photolysis of Tetraphenylhydrazine in an SDS Micelle: Time Dependence of the Population of the Spin States. *J. Phys. Chem. A* **1997**, *101*, 7783−7786.

(54) Avdievich, N. I.; Forbes, M. D. E. Dynamic Effects in Spin-Correlated Radical Pair Theory: J Modulation and a New Look at the Phenomenon of Alternating Line Widths in the EPR Spectra of Flexible Biradicals. *J. Phys. Chem. A* **1995**, *99*, 9660−9667.

(55) Kobori, Y.; Fuki, M.; Murai, H. Electron Spin Polarization Transfer to the Charge-Separated State from Locally Excited Triplet Configuration: Theory and Its Application to Characterization of Geometry and Electronic Coupling in the Electron Donor-Acceptor System. *J. Phys. Chem. B* **2010**, *114*, 14621−14630.

(56) Gonen, O.; Levanon, H. Time-resolved EPR spectroscopy of electron spin polarized ZnTPP triplets oriented in a liquid crystal. *J. Phys. Chem. B* **1985**, *89*, 1637−1643.

(57) Gouterman, M.; Khalil, G.-E. Porphyrin free base phosphorescence. *J. Mol. Spectrosc.* **1974**, *53*, 88−100.

(58) Song, Y.; Clafton, S. N.; Pensack, R. D.; Kee, T. W.; Scholes, G. D. Vibrational Coherence Probes the Mechanism of Ultrafast Electron Transfer in Polymer-Fullerene Blends. *Nat. Commun.* **2014**, *5*, No. 4933.

(59) Ohta, K.; Tominaga, K.; Ikoma, T.; Kobori, Y.; Yamada, H. Microscopic Structures, Dynamics, and Spin Configuration of the Charge Carriers in Organic Photovoltaic Solar Cells Studied by Advanced Time-Resolved Spectroscopic Methods. *Langmuir* **2022**, *38*, 7365−7382.

(60) Marcus, R. A.; Sutin, N. Electron transfer in chemistry and biology. *Biochim. Biophys. Acta, Rev. Bioenerg.* **1985**, *811*, 265−322.

(61) Kobori, Y.; Sekiguchi, S.; Akiyama, K.; Tero-Kubota, S. Chemically Induced Dynamic Electron Polarization Study on the Mechanism of Exchange Interaction in Radical Ion Pairs Generated by Photoinduced Electron Transfer Reactions. *J. Phys. Chem. A* **1999**, *103*, 5416−5424.

(62) Valiev, R. R.; Cherepanov, V. N.; Artyukhov, V. Y.; Sundholm, D. Computational studies of photophysical properties of porphin, tetraphenylporphyrin and tetrabenzoporphyrin. *Phys. Chem. Chem. Phys.* **2012**, *14*, 11508−11517.

(63) Gould, I. R.; Young, R. H.; Mueller, L. J.; Albrecht, A. C.; Farid, S. Electronic Structures of Exciplexes and Excited Charge-Transfer Complexes. *J. Am. Chem. Soc.* **1994**, *116*, 8188−8199.

(64) Carmieli, R.; Smeigh, A. L.; Conron, S. M. M.; Thazhathveetil, A. K.; Fuki, M.; Kobori, Y.; Lewis, F. D.; Wasielewski, M. R. Structure and Dynamics of Photogenerated Triplet Radical Ion Pairs in DNA Hairpin Conjugates with Anthraquinone End Caps. *J. Am. Chem. Soc.* **2012**, *134*, 11251−11260.

(65) Merces, L.; Candiotto, G.; Ferro, L. M. M.; de Barros, A.; Batista, C. V. S.; Nawaz, A.; Riul, A., Jr; Capaz, R. B.; Bufon, C. C. B. Reorganization Energy upon Controlled Intermolecular Charge-Transfer Reactions in Monolithically Integrated Nanodevices. *Small* **2021**, *17*, No. 2103897.

(66) McConnell, H. M. Intramolecular Charge Transfer in Aromatic Free Radicals. *J. Chem. Phys.* **1961**, *35*, 508−515.

(67) Tong, G. S. M.; Kurnikov, I. V.; Beratan, D. N. Tunneling Energy Effects on GC Oxidation in DNA. *J. Phys. Chem. B* **2002**, *106*, 2381−2392.

(68) Kuroda, S.-i.; Marumoto, K.; Sakanaka, T.; Takeuchi, N.; Shimoi, Y.; Abe, S.; Kokubo, H.; Yamamoto, T. Electron-nuclear double-resonance observation of spatial extent of polarons in polythiophene and poly(3-alkylthiophene). *Chem. Phys. Lett.* **2007**, *435*, 273−277.

(69) Fuhs, M.; Elger, G.; Mobius, K.; Osintsev, A.; Popov, A.; Kurreck, H. Multifrequency time-resolved EPR (9.5GHz and 95GHz) on covalently linked porphyrin-quinone model systems for photo-synthetic electron transfer: effect of molecular dynamics on electron spin polarization. *Mol. Phys.* **2000**, *98*, 1025−1040.

(70) Privitera, A.; Grüne, J.; Karki, A.; Myers, W. K.; Dyakonov, V.; Nguyen, T.-Q.; Riede, M. K.; Friend, R. H.; Sperlich, A.; Gillett, A. J. Geminate and Nongeminate Pathways for Triplet Exciton Formation in Organic Solar Cells. *Adv. Energy Mater.* **2022**, *12*, No. 2103944.

📖 Recommended by ACS